



**A Complete Breast Cancer Detection Approach Via Quantitative
and Qualitative Analysis of Breast Ultrasound (BUS) Images**

By

Irteza Enan Kabir

Student ID – 132418

Abdullah Salmon Ashik

Student ID – 132415

Rasheed Abid

Student ID - 132436

A thesis submitted to Islamic University of Technology
B.Sc. in Electrical and Electronic Engineering

Supervisor

Prof. Dr. Kazi Khairul Islam

Professor

Department of EEE, IUT, Board Bazar, Gazipur-1704.

Certificate of Approval

The thesis titled “A Complete Breast Cancer Detection Approach Via Quantitative and Qualitative Analysis of Breast Ultrasound (BUS) Images.” submitted by Irteza Enan Kabir, Abdullah Salmon Ashik and Rasheed Abid bearing Student No. 132418, 132415, 132436 respectively of Academic Year 2016-2017 has been found as satisfactory and accepted as partial fulfillment of the requirement for the degree of Bachelor of Science in Electrical and Electronic Engineering on, 2017.

Dr. Kazi Khairul Islam
Professor

(Supervisor)

Department of Electrical and Electronic Engineering
Islamic University of Technology
Board Bazar, Gazipur-1704, Bangladesh.

Dedication

This thesis is dedicated to our beloved parents and all our well-wishers helping us to accomplish this work.

Acknowledgment

First of all, I would like express my heartiest gratitude to the Almighty Allah for providing me the strength to complete this thesis work. After the Almighty, it is my great pleasure to express gratitude to the people who made this thesis possible.

Foremost, I would like to express my deepest gratitude to my supervisor, Prof. Dr. Kazi Khairul Islam, PhD, Dept. of EEE, IUT whose expertise, understanding and patience, added significantly to my graduate experience. This study could have never been done without my supervisors' motivation, guidance and inspiration.

I would also like to thank my mentor and Co-supervisor Dr. S. Kaisar Alam, Adjunct Professor, Rutgers University, NJ who sacrificed his valuable time for continuously guiding and motivating me for completing the thesis. He taught me how to work with the medical ultrasound imaging system and introduced me with the philosophical aspect of research which I will carry with me for the rest of my life.

I would like to acknowledge Dr. Juan Shan, Assistant Professor, Pace University, NY, USA, Prof. Dr. Dimitris Metaxas, Professor, Rutgers University, NJ, USA and Dr. Brian S. Garra. M.D., FDA, Silver Spring, MAD, USA for a number of stimulating discussions on the thesis. They enriched my understandings regarding the topic by sharing their valuable knowledge.

I would like express my heartfelt gratitude to Prof. Dr. Md. Ashraful Hoque, Head, Dept. of EEE. I would like to thank all the faculty members of EEE Dept., IUT for their continuous support and encouragement.

Abstract

Globally, cancer is becoming a major health issue as advances in modern medicine continue to extend the human life span. In the U.S., cancer is the second most-common cause of death, exceeded only by heart disease and accounting for nearly one of every four deaths. Breast cancer ranks second as a cause of cancer death in women (after lung cancer).

Thus, early detection and treatment are critical in reducing breast cancer related mortality.

Working with Breast ultrasound (BUS) data or image is regarded as a challenging task due to the inherent nature of ultrasound imaging. Ultrasound imaging is characterized by speckle patterns, anisotropy and signal drop-out. Moreover, proper image acquisition techniques by the clinicians and their level of expertise also play a dominant role in determining the image quality. The fuzziness in the shape and boundaries of the breast lesions make it very difficult to automate the segmentation of BUS images. In order to improve the issues prevalent in the existing approaches, a complete qualitative and quantitative analysis of Breast ultrasound (BUS) images is proposed in this thesis. The method involves three steps – (a) Finding out strain image by means of strain estimation, (b) Final Segmentation of the detected lesion and (c) Quantitative analysis of the lesion.

Table of Contents

Acknowledgment	ii
Abstract	iii
Table of Contents	iv
Acronyms	vii
List of Tables	viii
List of Figures	i
1 Introduction	01
1.1 Breast Cancer Scenario	01
1.2 Medical Imaging in Breast Cancer Detection	01
1.2.1 Mammography	01
1.2.2 Magnetic Resonance Imaging (MRI)	03
1.2.3 Ultrasound Imaging	05
1.3 Thesis Objectives	08
1.4 Thesis Organization	09
2 Background	09
2.1 Related Work	10
2.2 Overview of the proposed method	10
3 Strain Estimation	12
3.1.1 Segmentation of signal columns	13
3.1.2 Lateral movement of tissue	14

3.1.3	Finding displacement and then strain from displacement:-----	15
3.2	BUS Dataset:-----	16
3.3	Experimental Results-----	16
4	Breast Lesion Segmentation-----	23
4.1	Image Pre-processing for Segmentation -----	25
4.1.1	Speckle Reduction -----	26
4.1.2	Potential Energy Image formation -----	27
4.1.3	Phase in Maximum Orientation (PMO) Image Formation -----	28
4.1.4	Final Processed Image Formation -----	30
4.2	Edge Map improvement by Two-Pointers -----	31
4.2.1	Initialization region near the seed point-----	31
4.2.2	Breaking the Histogram of the Total Image-----	31
4.3	Initial Segmentation using Region Growing-----	33
4.4	Final Segmentation -----	37
4.4.1	Graph Cuts Segmentation-----	38
4.4.2	GrowCut Segmentation -----	39
4.4.3	Metamorphs and Deforming Segmentation-----	40
4.4.4	Automatic Training Pixel Generation for Segmentation-----	41
4.5	Final Segmentation using GraphCut and GrowCut-----	43
5	Quantitative Ultrasound -----	55

5.1.1	Introduction-----	55
5.1.2	Basic Functionalities -----	56
5.1.3	background and motivation-----	56
5.2.1	Overview -----	58
5.2.1.1	Homodyne K-----	58
5.2.1.2	Nakagami Distribution -----	59
5.3.1	Theory -----	60
5.3.1.1	homodyne K -----	60
5.3.1.2	Nakagami Distribution -----	62
5.4.1	Process and results -----	68
5.4.1.1	homodyne K -----	68
5.4.1.1.1	RSK-----	69
5.4.1.2	Nakagami Distribution-----	72
5.4.1.1.2	method -----	73
6	Conclusion and Future Directions for Research-----	78
7	References -----	79

Acronyms

B-mode	Brightness-mode
CAD	Computer Aided Diagnosis
FP	False Positive
FN	False Negative
MRI	Magnetic Resonance Imaging
ROI	Region of Interest
TP	True Positive
US	Ultrasonography
QUS	Quantitative Ultrasound

List of Figures

Figure 1-1 A typical breast mammogram (Image courtesy: Radiological Society of North America)	2
Figure 1-2 An illustration of a real MRI scanner.....	3
Figure 1-3 A Breast MRI with False Positive Nodule (Image courtesy: Radiological Society of North America)	4
Figure 1-4 Basic Pulse-Echo Ultrasound System (Image Courtesy: Dr. S. Kaisar Alam, Rutgers University, NJ, USA)	6
Figure 1-5 B-mode image formation (Image Courtesy: Dr. S. Kaisar Alam, Rutgers University, NJ, USA)	6
Figure 2-1 Overview of the proposed method	11
Figure 3-1 Segmentation of Signal Columns	13
Figure 3-2 Lateral Movement of Tissue	14
Figure 3-3 Finding Out the Lateral Shift of Data Stream	15
Figure 3-4 Processed data at low applied strain (2 %):.....	17
Figure 3-5 Processed data at 4% applied strain	18
Figure 3-6 Processed data at 6% applied strain	19
Figure 3-7 Processed data at 8% applied strain.....	20
Figure 3-8 Processed data at 12% applied strain	21

Figure 4-1 Overview of Segmentation Framework	24
Figure 4-2 Flowchart of image pre-processing for final segmentation.....	25
Figure 4-3 (a) Original Image. (b) Speckle Reduced Image	27
Figure 4-4 (a) De-noised Image. (b) PMO image.....	29
Figure 4-5 (a) Original Image. (b) Pre-processed Image	30
Figure 4-6 - Two Pointers processing step to obtain intermediate image with snake segmentation model.....	32
Figure 4-7 Column 1 - Original Image with manual delineation. Column 2- Region Growing using Madabhushi's method [14].....	34
Figure 4-8 (a) Original Image with leaked edge indicated with a yellow arrow. (b) Region Growing result by Shan's method [9].....	35
Figure 4-9 (a) Original Image. (b) Result of Region Growing proposed in this thesis	37
Figure 4-10 (a) Original Image. (b) Region Growing. (c) Foreground Region. (d) Background Region	42
Figure 4-11 (a) Original Image with seed point and manual delineation (b) Segmentation Result using GraphCut.	43
Figure 4-12 (a) Original Image with seed point and manual delineation (b) Segmentation Result using GrowCut.....	44
Figure 5-1 backscattering of signal.	58
Figure 5-2 Typical examples of the homodyned K-distribution	61
Figure 5-3 scattering media	69
Figure 5-4 μ vs K curve for different part of the tissue.....	71
Figure 5-5 nakagami distribution.....	72

Figure 5-6 boundary points	73
Figure 5-7 Boundary detection	74
Figure 5-8 region of interest	75
Figure 5-9 effective number of scatterer comparison	76

1 Introduction

1.1 Breast Cancer Scenario

Breast cancer is the most common and the second-most lethal cancer among females worldwide [1]. Among the women only in USA, breast cancer alone is expected to account for 29% of all the new cancer diagnoses with an estimate of 246,660 cases in 2016 [2]. Breast cancer survival rates vary greatly worldwide, ranging from 80% or over in North America, Sweden and Japan to around 60% in middle-income countries and below 40% in low-income countries [3]. Statistics reveals that if breast cancer is diagnosed at a localized stage then the 5-year relative survival rate approaches to 99% [4]. Since the causes of breast cancer still remain unknown, early detection and treatment of breast cancer is the top most priority in reducing breast cancer related mortality.

1.2 Medical Imaging in Breast Cancer Detection

Current methods for detecting and diagnosing breast cancer includes mammography, ultrasound imaging and magnetic resonance imaging (MRI). In this section, the standard imaging modalities for early detection of breast cancer is discussed.

1.2.1 Mammography

Mammography is considered as the standard imaging method for earlier detection and diagnosis of breast cancer [5, 6]. It is specialized medical imaging that uses a low-dose x-ray system to see inside the breasts. Two schemes of mammography is used in breast cancer detection and diagnosis namely Screening Mammography and Diagnostic Mammography. Typically, the first step in breast cancer detection is screening mammography which is a

low-dose X-ray examination on asymptomatic women. Diagnostic mammography is an X-ray examination done to evaluate a breast complaint or to investigate an abnormality found during a physical examination or during screening mammography. A typical breast mammogram is shown in Figure 1-1.

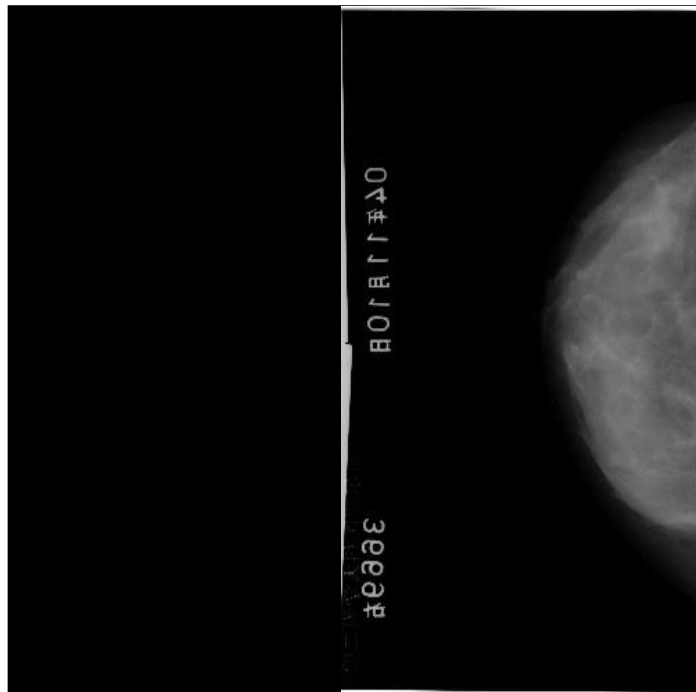


Figure 1-1 A typical breast mammogram (Image courtesy: Radiological Society of North America)

However, mammography suffers from different limitations such as low specificity of in case of adolescent women with dense breast [5] and potential risk towards patients' health due to ionizing radiation [7]. Many unnecessary (65–85%) biopsy operations are due to the low specificity of mammography. The unnecessary biopsies not only increase the cost, but also cause emotional suffering for the patients.

1.2.2 Magnetic Resonance Imaging (MRI)

Magnetic resonance imaging is a medical imaging technique used in radiology to investigate the anatomy and physiology of the body during both health and disease states. MRI scanners employ magnetic fields and radio waves to form images of the body. The technique is widely used in hospitals for medical diagnosis and, the staging of diseases and to perform follow-ups without causing exposure to ionizing radiation. A real MRI scanner is shown Figure 1-2.



Figure 1-2 An illustration of a real MRI scanner

Breast MRI has a number of different uses for breast cancer, including:

- Screening high-risk women (women known to be at higher than average risk for breast cancer, either because of a strong family history or a gene abnormality)
- Gathering more information about an area of suspicion found on a mammogram or ultrasound

- Monitoring for recurrence after treatment

Although breast MRI is a more sensitive test than mammography in many ways, this increased sensitivity may cause areas of the breast that do not have cancer to appear abnormal, producing an increased number of false-positive test results. False-positive test results indicate cancer when no cancer is actually present. A breast MRI with false positive nodule is illustrated in Figure 1-3. This false-positive results may lead to unnecessary biopsies (removal of breast tissue for further study) and increased anxiety for many women. At the same time, breast MRI cannot visualize the calcium deposits, known as calcifications or microcalcifications, which typically surround DCIS lesions (the suspicious area). Mammography, on the other hand, can detect these calcium deposits accurately. Finally, breast MRI is more expensive than mammography.

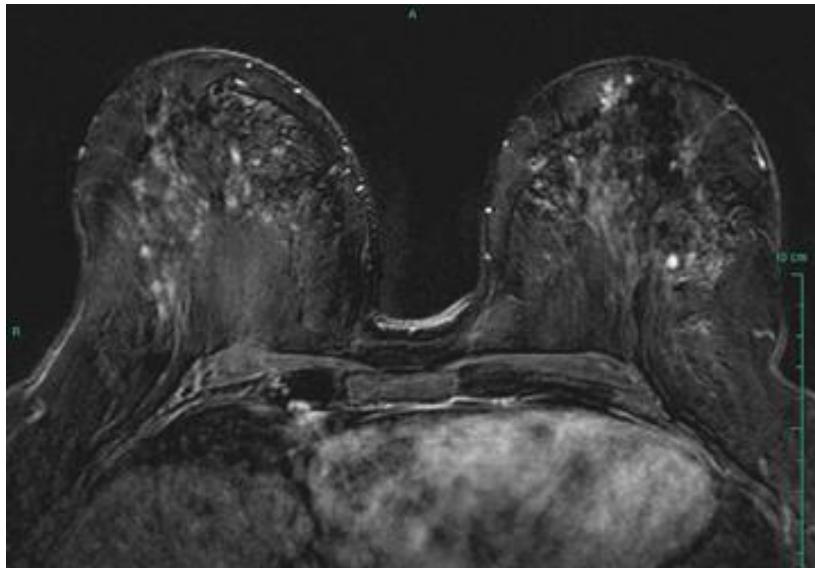


Figure 1-3 A Breast MRI with False Positive Nodule (Image courtesy: Radiological Society of North America)

1.2.3 Ultrasound Imaging

Ultrasound imaging also known as ultrasonography or simply sonography, uses high-frequency sound waves to view the internal regions of the body. It is the most economical and widely available medical imaging modality. Because ultrasound images are captured in real-time, they can also show the movements of the body's internal organs as well as the blood's passage through the blood vessels. Unlike X-ray imaging, no ionizing radiation exposure is associated with ultrasound imaging. Nowadays it is extensively used in fetal imaging, cardiac imaging, breast cancer detection, and detection of benign and malignant tissue in the human body.

1.2.3.1 Basic Principle of B-Mode Ultrasound

Modern medical US is performed primarily using a pulse-echo approach with a brightness-mode (B-mode) display. The basic principles of B-mode imaging are much the same today as they were several decades ago. This involves transmitting small pulses of ultrasound into the body from a transducer. As the ultrasound waves penetrate body tissues of different acoustic impedances along the path of transmission, some are reflected back to the transducer (echo signals) and some continue to penetrate deeper. The echo signals returned from many sequential coplanar pulses are processed (generating the envelope from echo signal) and combined to generate an image. Thus, an ultrasound transducer works both as a speaker (generating sound waves) and a microphone (receiving sound waves). An overview of the image acquisition using ultrasound is presented in Figure 1-4 and Figure 1-5. The ultrasound pulse is in fact quite short, but since it traverses in a straight path, it is often referred to as an ultrasound beam. The direction of ultrasound propagation along the beam line is called the axial direction, and the direction in the image

plane perpendicular to axial is called the lateral direction. Usually only a small fraction of the ultrasound pulse returns as a reflected echo after reaching a body tissue interface, while the remainder of the pulse continues along the beam line to greater tissue depths.

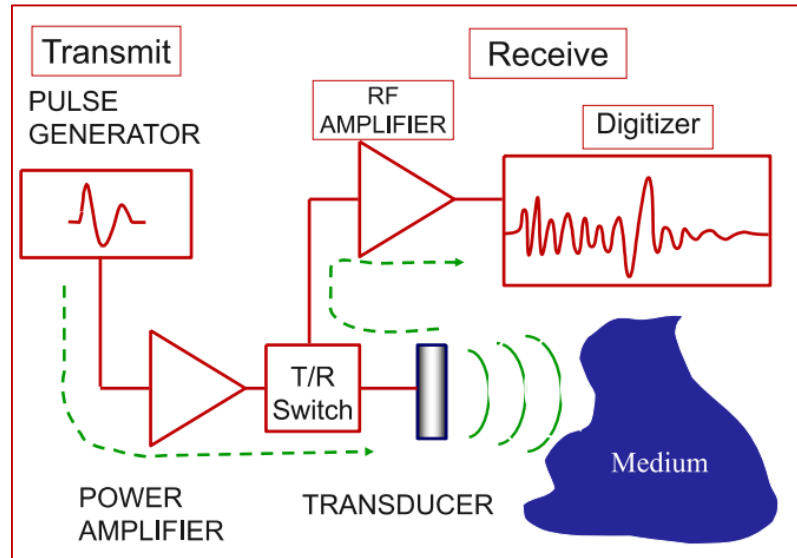


Figure 1-4 Basic Pulse-Echo Ultrasound System (Image Courtesy: Dr. S. Kaisar Alam, Rutgers University, NJ, USA)

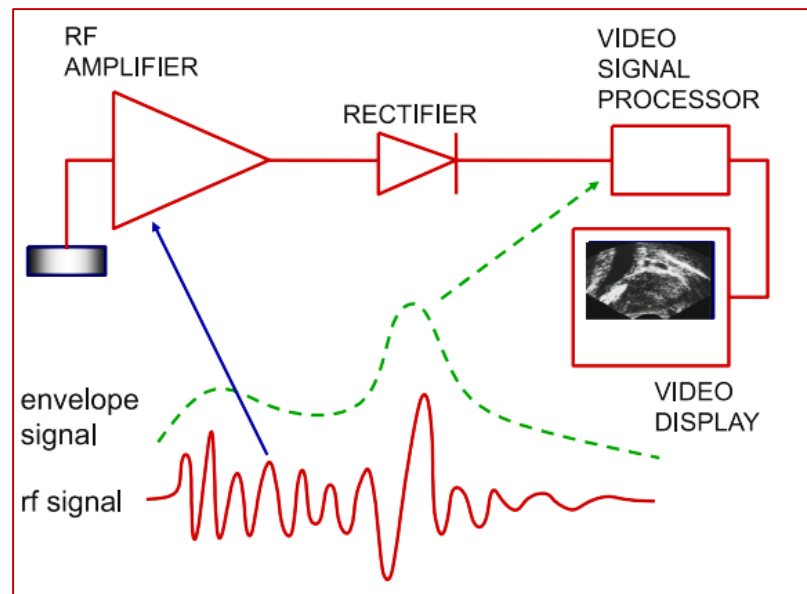


Figure 1-5 B-mode image formation (Image Courtesy: Dr. S. Kaisar Alam, Rutgers University, NJ, USA)

1.2.3.2 Challenges in Ultrasound Image Interpretation

Image artifacts are commonly encountered in clinical ultrasonography (US) and may be a source of confusion for the interpreting physician and for computer based systems. Some artifacts may be avoidable and arise secondary to improper scanning technique. Other artifacts are generated by the physical limitations of the modality. US artifacts can be understood with a basic appreciation of the physical properties of the ultrasound beam, the propagation of sound in matter, and the assumptions of image processing. US artifacts arise secondary to errors inherent to the ultrasound beam characteristics, the presence of multiple echo paths, velocity errors, and attenuation errors. The beam width, side lobe, reverberation, comet tail, ring-down, mirror image, speed displacement, refraction, attenuation, shadowing, and increased through transmission artifacts are encountered routinely in clinical practice. Recognition of these artifacts is important because they may be clues to tissue composition and aid in diagnosis. The ability to recognize and remedy potentially correctable US artifacts is important for image quality improvement and optimal patient care.

1.2.3.3 Ultrasound imaging in Breast Cancer Detection

To address the issues of mammography and breast MRI, ultrasound imaging is considered to be one of the most effective tools as an adjunct to it [7]. Statistics show that more than one out of every four study on breast cancer detection is based on ultrasound images, and the proportion is rapidly increasing [8, 9]. Studies have demonstrated that using US images can discriminate benign and malignant masses with a high accuracy [10]. Use of ultrasound can increase over all cancer detection by 17% [11] and reduce the number of unnecessary biopsies by 40% which can save as much as \$1 billion per year in the United States alone.

Breast ultrasound (BUS) imaging is superior to mammography in the following ways. (1) Since it requires no radiation, ultrasound examination is more convenient and safer than mammography for patients and radiologists in daily clinical practice [12]. It is also cheaper and faster than mammography. Thus, ultrasound is especially suitable for the low-resource countries indifferent continents. (2) Ultrasound techniques are more sensitive than mammography for detecting abnormalities in dense breasts; hence, it is more valuable for women younger than 35 years of age [11]. (3) There is a high rate of false positives in mammography which causes a lot of unnecessary biopsies. In contrast, the accuracy rate of BUS imaging in the diagnosis of simple cysts is much higher [10]. Thus, US imaging has become one of the most important diagnostic tools for breast cancer detection.

1.3 Thesis Objectives

The context of this thesis work is a complete A Complete Breast Cancer Detection Approach via Quantitative and Qualitative Analysis of Breast Ultrasound (BUS) Images

This includes qualitative analysis by strain estimation method, then accurate breast lesion segmentation in US images and lastly quantitative analysis of those images. Therefore, the objective of this thesis work was to develop more robust, accurate and automatic breast lesion depiction, segmentation, quantitative analysis and then diagnosis method for ultrasound images.

The outcome of this thesis will facilitate the complete diagnosis of breast cancer.

1.4 Thesis Organization

The thesis is organized in the following way –

Chapter 2 (Background) presents the literature review and state-of-art situation of problem.

Chapter 3 Strain Estimation from Breast Ultrasound (BUS) data.

Chapter 4 Breast Lesion Segmentation

Chapter 5 Quantitative Ultrasound

Chapter 6 (Conclusion and Future Directions for Research) summarizes the whole thesis work and presents the future scope of research in BUS image segmentation problem.

2 Background

2.1 Related Work

Several articles are found to address the problem of strain estimation using Breast Ultrasound (BUS) Images. Over the past several years, methods based on tissue elasticity have gained significance for diagnosis of disease [18]–[26]. These methods fall into two main groups: methods where a low frequency vibration is applied to the tissue and the resulting behavior is inspected [18]–[21], [24], and methods where a compression is

applied to the tissue and the resulting strain is estimated [22], [23]. Among the first group of techniques, in sonoelasticity imaging [19], [20], the vibration amplitude pattern of the shear waves in the tissue under investigation is detected and a corresponding color image (similar to color Doppler display) is superimposed on the conventional grayscale image. A theory of sonoelasticity imaging was developed [25] and in vitro results on excised human prostate were promising [26]. Among the techniques based on the estimation of tissue strain, elastography [22] is based on estimating the tissue strain using a correlation algorithm, whereas another elasticity imaging technique is based on estimating such strain using the phase information [23]. In elastography, the local tissue displacements are estimated from the time delays between gated pre- and postcompression echo signals, whose axial gradient is then computed to estimate the local strain.

For QAS many sources were used for Classification of Ultrasonic B-Mode Images of Breast Masses[38]. Review of Envelope Statistics Models for Quantitative Ultrasound Imaging and Tissue Characterization and review of Quantitative Ultrasound: Envelope Statistics and Backscatter Coefficient Imaging and Contributions to Diagnostic Ultrasound for mathematical model of the distributions[39][40] .

2.2 Overview of the proposed method

. Overview of the proposed method can be broken into three steps. Firstly, strain estimation and finding out the lesion, then segmentation and lastly qualitative analysis.

The flow chart of the proposed method is presented in Figure 2-1.

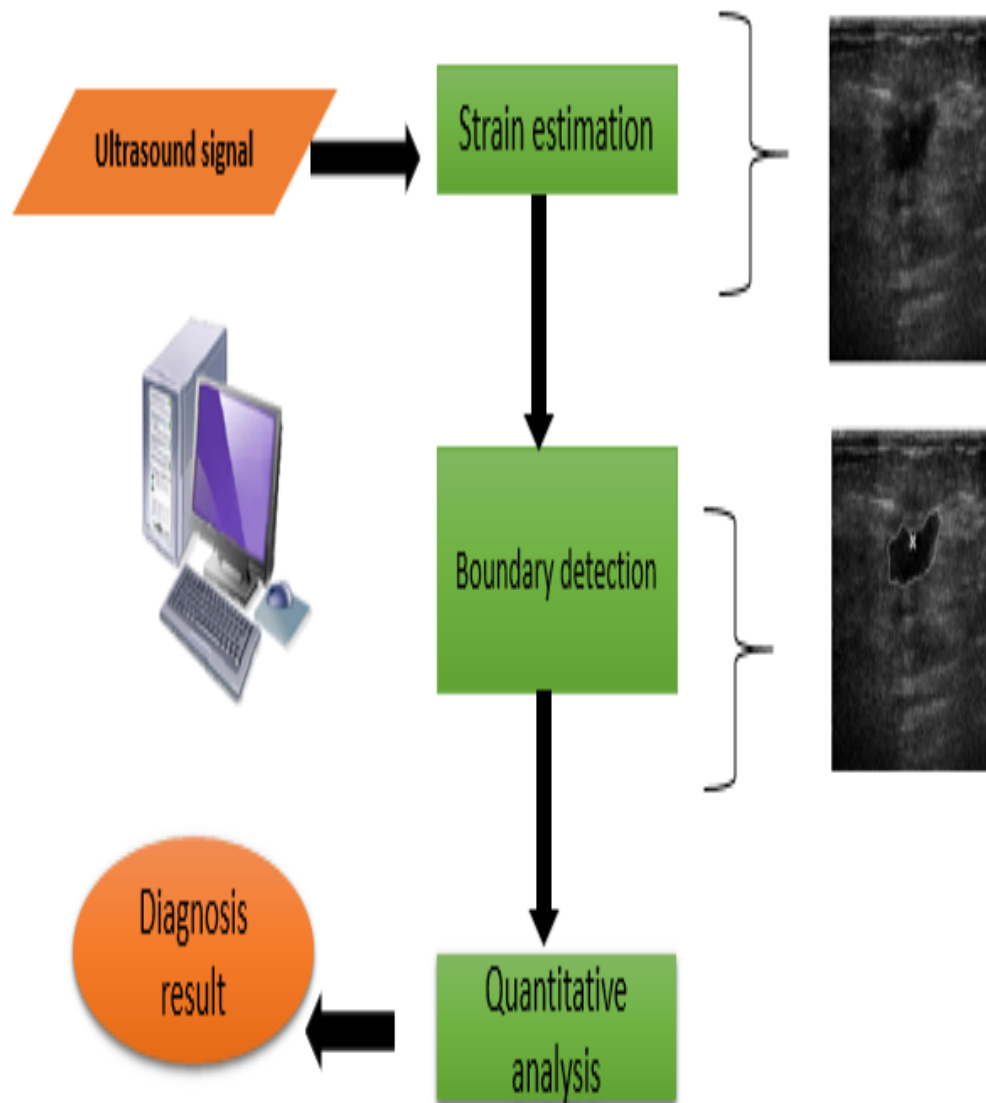


Figure 2-1 Overview of the proposed method

3 STRAIN ESTIMATION from Breast Ultrasound (BUS) data:

In this chapter, we discuss our proposed framework of strain estimation.

Several strain estimation techniques in elastography have been developed over the last 10 years. Time-domain methods typically estimate the axial strain as the gradient of the displacement (time-delay) estimates obtained using crosscorrelation of precompression and temporally stretched postcompression radiofrequency (RF) A-line segments (Cespedes and Ophir 1993; Varghese and Ophir 1997a; Ophir et al. 1999). Some of the alternative strain estimation methods include 2-D companding and sum-absolute-difference estimators (Chaturvedi et al. 1998), lateral strain estimation (Konofagou and Ophir 1998), Fourier-based speckle phase-tracking (O'Donnell et al. 1991), wavelet-based strain estimation (Bilgen 1999), adaptive strain estimation (Alam et al. 1998; Brusseau et al. 2001; Srinivasan et al. 2002b), strain estimation using staggered windows (Srinivasan et al. 2002b), zero-crossing tracking (Srinivasan and Ophir 2003) and incoherent estimators based on the power spectrum, such as centroid tracking (Konofagou et al. 1999; Varghese et al. 2000), spectral cross-correlation (Varghese et al. 2000), spectral scaling (Alam et al. 2001) and optical flow-based techniques (Bertrand et al. 1984)

Changes in biological tissues change their elasticity. Elasticity imaging enjoys an ever increasing role in disease diagnosis. In elastography, tissue strain is estimated using signal processing. Strain is conventionally calculated from estimated displacements between the pre- and post-compression ultrasonic echo signals. In this paper, we introduce a novel 1.5D

strain estimator. The proposed algorithm uses 1D windows for fast computation, but searches in the lateral direction to account for non-axial motion.

3.1.1 Segmentation of signal columns

Pre and post-compression signals were segmented into overlapping 1D windows.

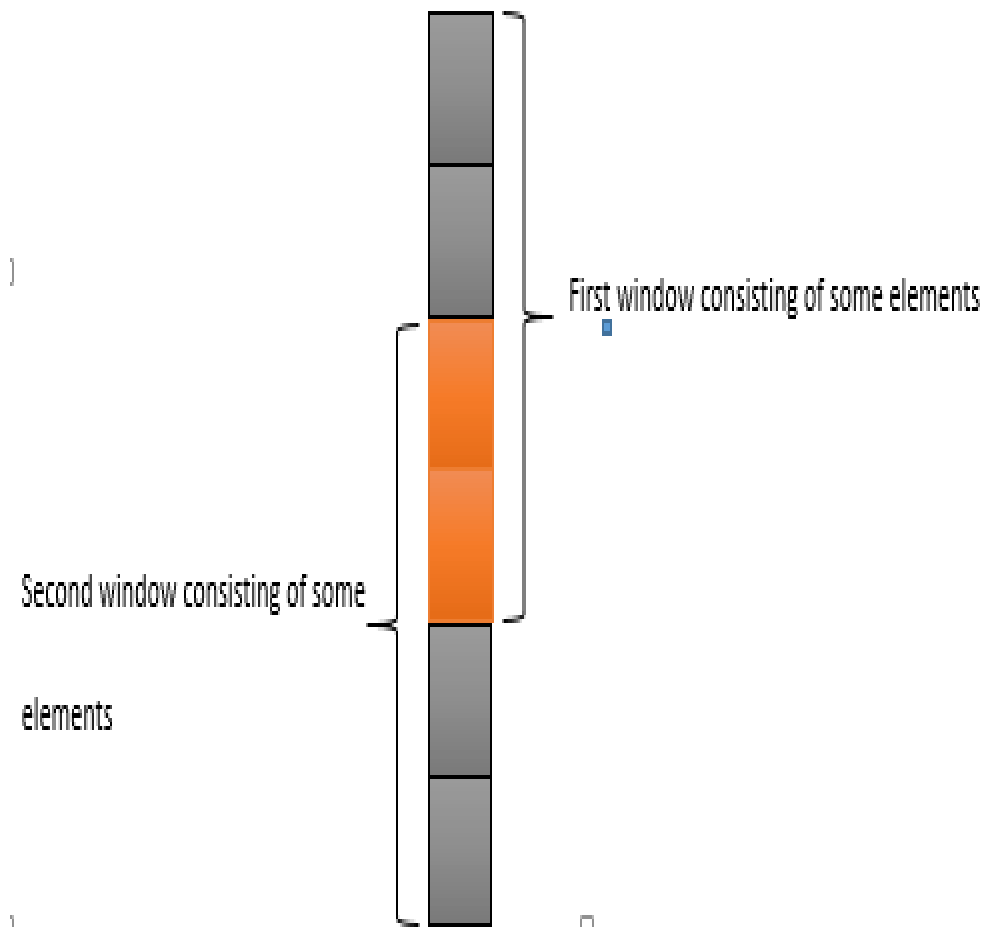


Figure 3-1: Segmentation of Signal columns

3.1.2 Lateral movement of tissue

When pressure is applied, different part of tissues deform differently. This happens more when high pressure or stress is applied. As a result, different tissue part may move laterally in different directions and the segments of the pre compression signal won't correspond to post compression signal in the exact Position.

Pre-compression echo signals were segmented into overlapping 1D windows. A segment from pre-compression i th column was correlated with the corresponding segments of $(i+n)$ th to $(i+n+1)$ th post-compression column. For each postcompression column, the maximum correlation was calculated, yielding $2n+1$ maximum correlation values. Then, we calculated which of these $2n+1$ correlation values is the highest; in other words, which lateral segment of the postcompression data had the highest correlation with the precompression data segment. If the pre-compression data segment (i th) had the highest correlation with the $(i+k)$ th postcompression data line segment, it meant that tissue deformed in such a way that the corresponding post-compression segment had shifted $+k$ columns.

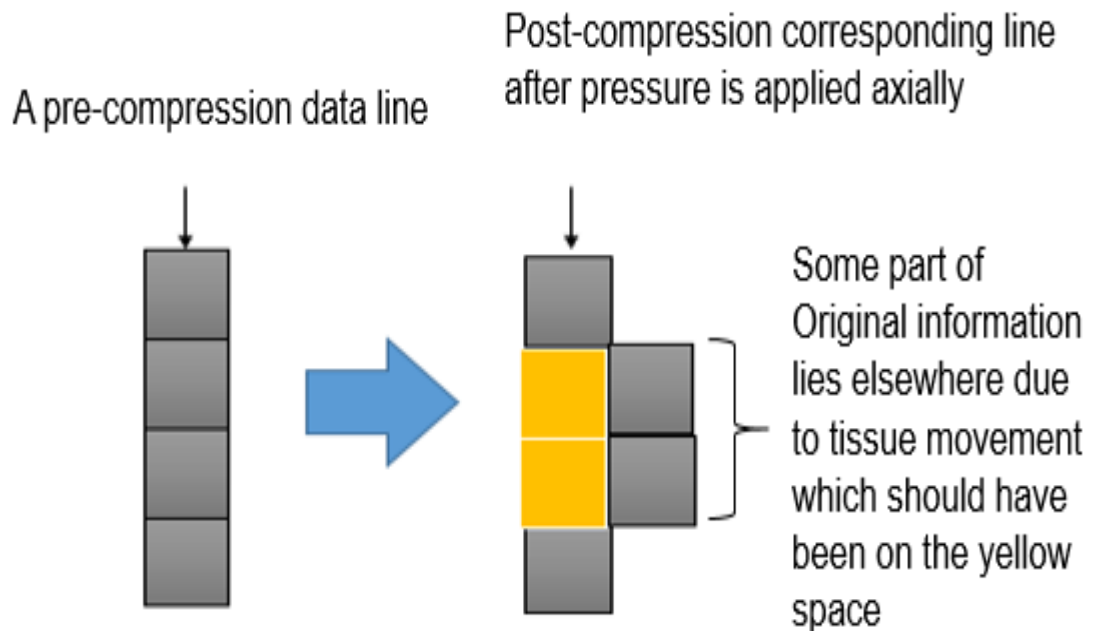


Figure 3-2: Lateral Movement of Tissue

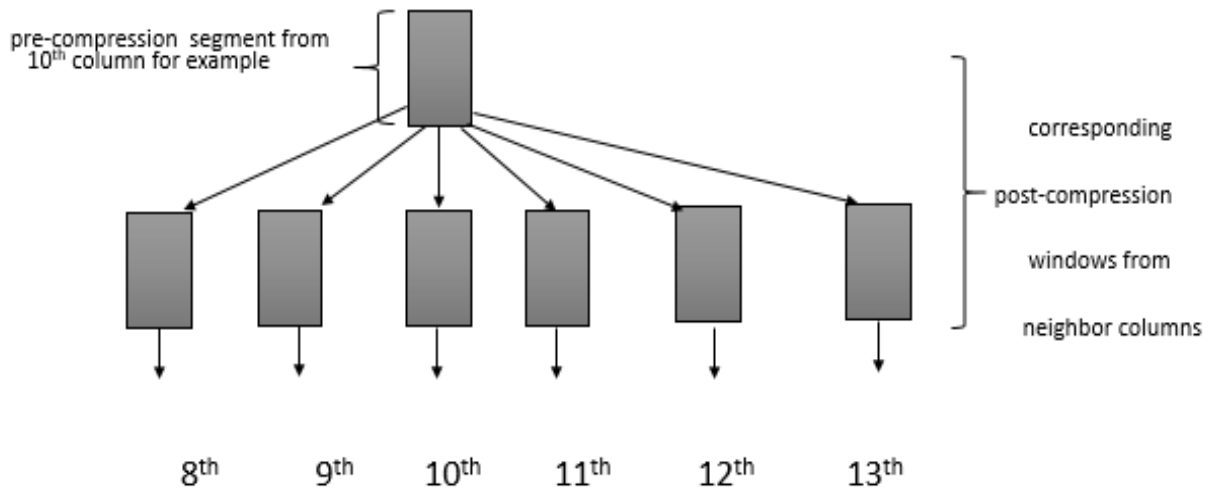


Figure 3-3: Finding out the lateral shift of data stream

3.1.3 Finding displacement and then strain from displacement:

In the time domain, the lags (displacements) between the segments of pre- and corresponding segments of postcompression signal was determined [8 from my paper].

First difference between two consecutive displacements gives strain [9].

Strain= (i,j)th displacement – (i+1,j)th displacement,

where, i=row and j=column.

The displacement map is computed by sliding the pre and post-compression windows and computing the displacement for each pre-compression window. The strain map is computed using the above equation [10]

3.2 BUS Dataset:

We have tested the proposed strain estimation method with the similar data used in [11], generated using 2-D finite element analysis. We used the software named Algor to simulate the phantom of 40 X 40 mm. The FEM model did not show out-of-plane motion as it was a 2D model. Total 30372 scatterers were used for the simulation. The phantom background was homogeneous and had 60 kPa stiffness. There were four circular inclusions, each having 7.5 mm diameter. The inclusions at the left bottom, top, bottom right and middle were respectively 10 dB, 20dB, 30dB and 40 dB stiffer than the background. A planar compressor compressed the phantom from the top. The phantom was scanned from the top using a transducer having 4 MHz center frequency and 60% bandwidth. There were total 128 scan lines. We added zero mean white noise to simulate sonographic SNR of 40 DB. There was also interaction between lesions which was responsible for the strain variations in the background, even though the phantom's background was a uniformly stiff background.

3.3 Experimental Results

We applied the proposed 1.5D strain estimation method on the conventional strain estimator, which calculates gradient of estimated displacements (no stretching) and on the adaptive stretching estimator. For both estimators, our approach significantly improved estimator performance.

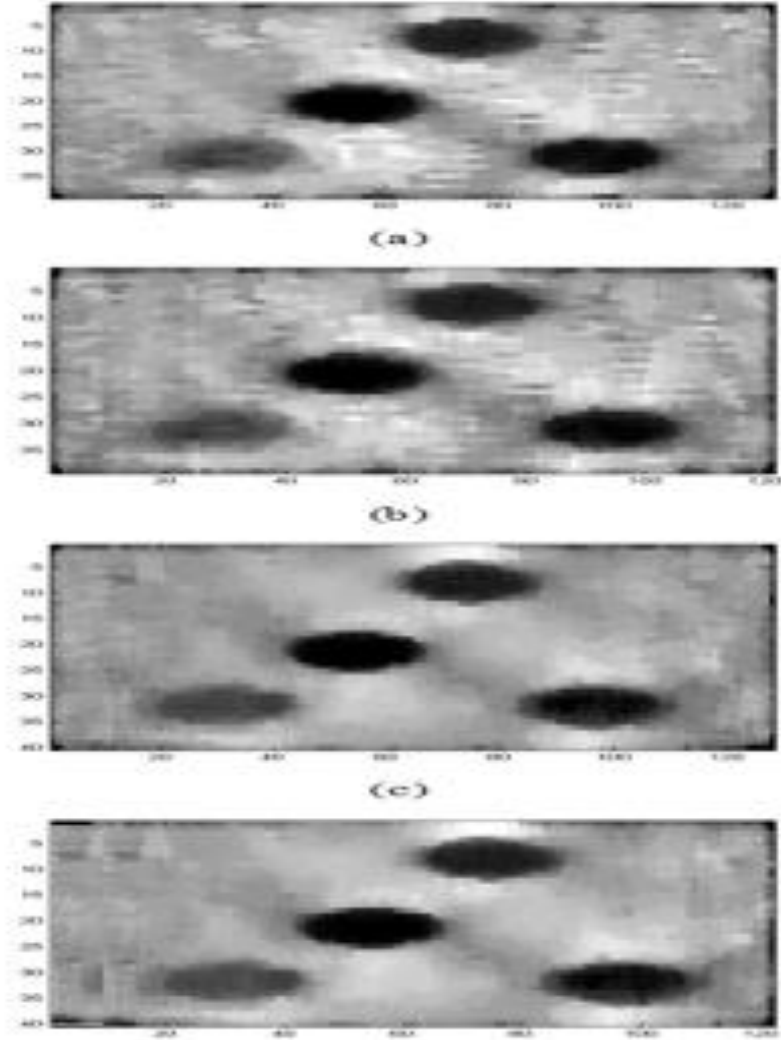


Figure 3-4 Processed data at low applied strain (2 %): (a)Gradient
 (b) 1.5D applied to gradient method (c) Adaptive stretching
 (d)Adaptive stretching with 1.5D

For applied strain of less than 4 percent, the result of our method is not very different from that of the conventional one. In Fig.3-3, we observe that the result for our method is better, or at worst, same. In these cases, we can assume that there was no significant shift of the post compression signal.

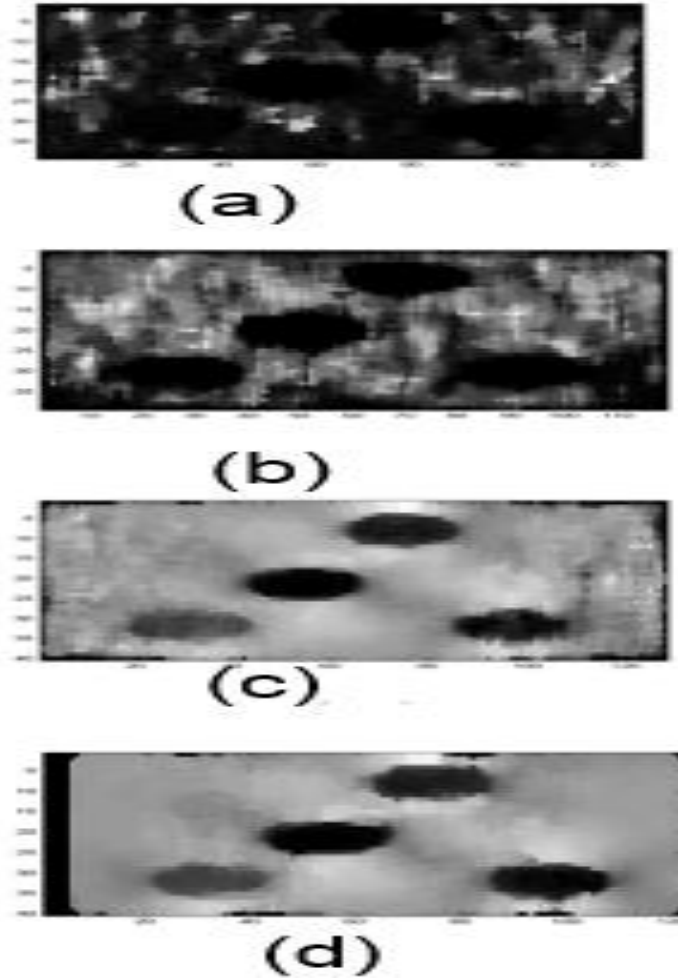


Figure 3-5 Processed data at 4% applied strain : (a)Gradient
 (b) 1.5D applied to gradient method (c) Adaptive stretching
 (d)Adaptive stretching with 1.5D

The 1.5D estimators show significantly better results when we use it on the FEM simulation data with applied strains of more than 4 percent, i.e. 6% or 8% applied strain.

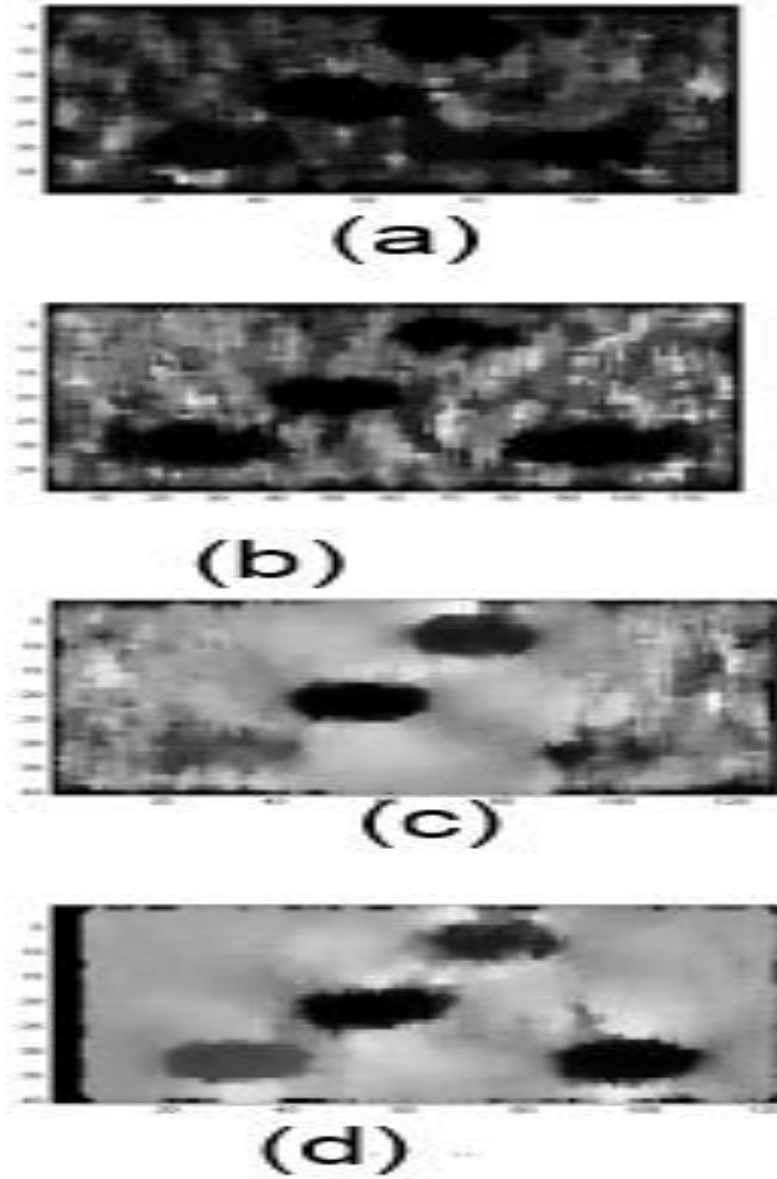


Figure 3-6 Processed data at 6% applied strain : (a)Gradient
(b) 1.5D applied to gradient method (c) Adaptive stretching
(d)Adaptive stretching with 1.5D

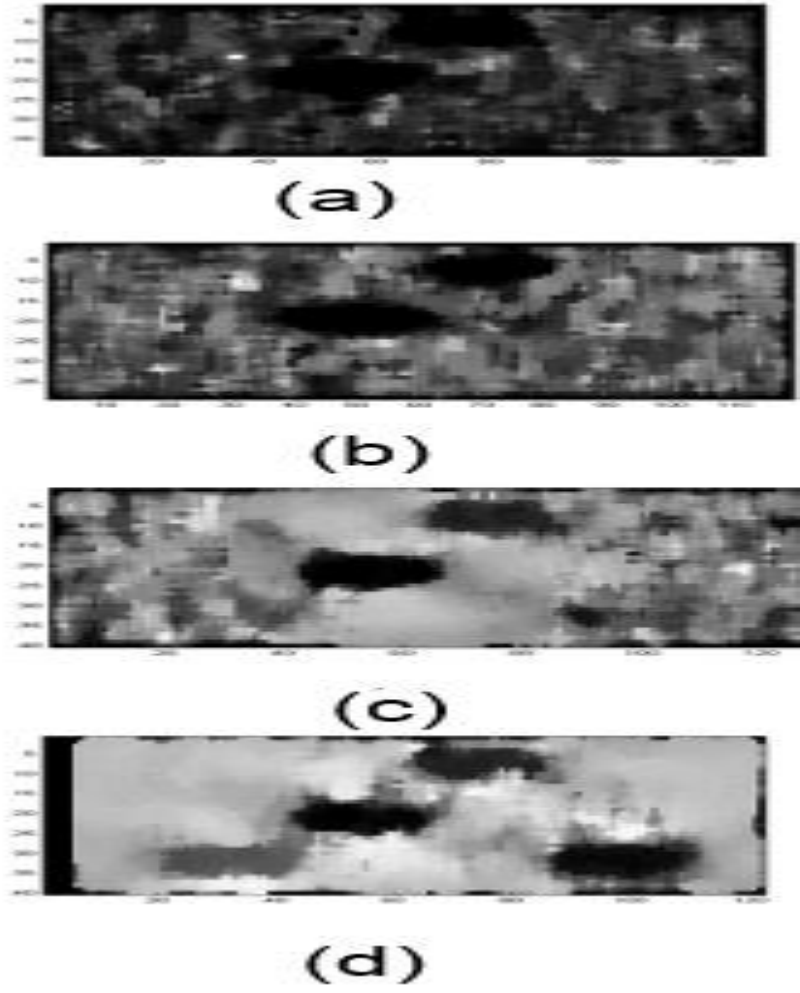


Figure 3-7 Processed data at 8% applied strain : (a)Gradient
(b) 1.5D applied to gradient method (c) Adaptive stretching
(d)Adaptive stretching with 1.5D

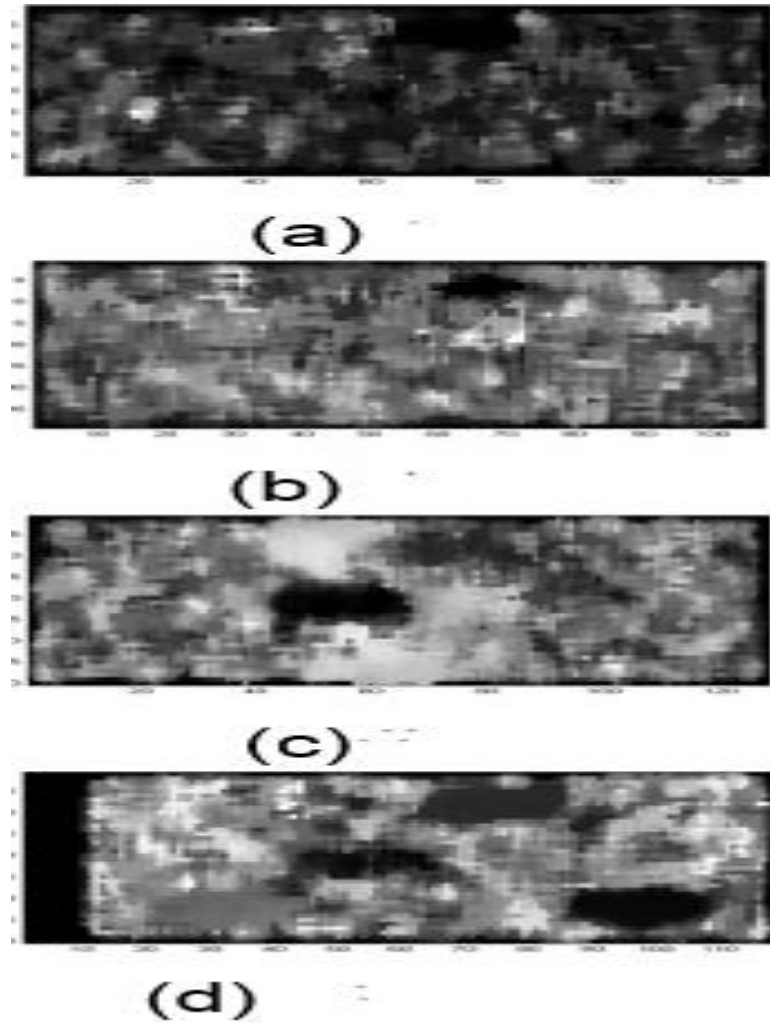


Figure 3-8 Processed data at 12% applied strain : (a)Gradient
 (b) 1.5D applied to gradient method (c) Adaptive stretching
 (d)Adaptive stretching with 1.5D

Fig. 3-5,3-6,3-7 and 3-8 shows elastograms for the same simulation for different applied strain levels. In the figure, we compared the original adaptive stretching and gradient methods with 1.5D processing applied to the same methods. It is quite evident from the figures that the proposed method improves performance. Especially for 6% and 8%

applied strain, homogeneous regions are not clear for the original methods, while our method successfully shows it.

The reason for our improvement is obvious, because post-compression signal is more likely to undergo lateral shifts when applied strain is higher. Our method takes this shift into account, ultimately producing a better strain image.

However, with higher applied strain, i.e. around 12 percent, the result becomes unusable for any original method. But for these cases, the proposed 1.5D method is able to provide comparatively better performance. In Figure 3-8, 1.5D with gradient method is somewhat better than its 1D counterpart. Adaptive stretching with 1.5D can depict all four inclusions, where original adaptive stretching method depicts only one.

4 Breast Lesion Segmentation

In this chapter, we describe the image map improvement techniques and final segmentation framework proposed for segmentation of breast lesion. Using histogram breakdown and simple image processing tools we improve the edge-map of the image in the initial case. Using the detected seed point, a coarse initial segmentation is achieved through a modified “Metamorph” image [27] segmentation. The result of the metamorphs is used as a guide for the training of segmentation tools. Finally, fine segmentation is achieved through “GraphCut” [28] and “GrowCut” [29] segmentation. To show the improvement in the method, we also show the results with the famous snake model as well. Overview of the segmentation framework is presented in Figure 4-1.

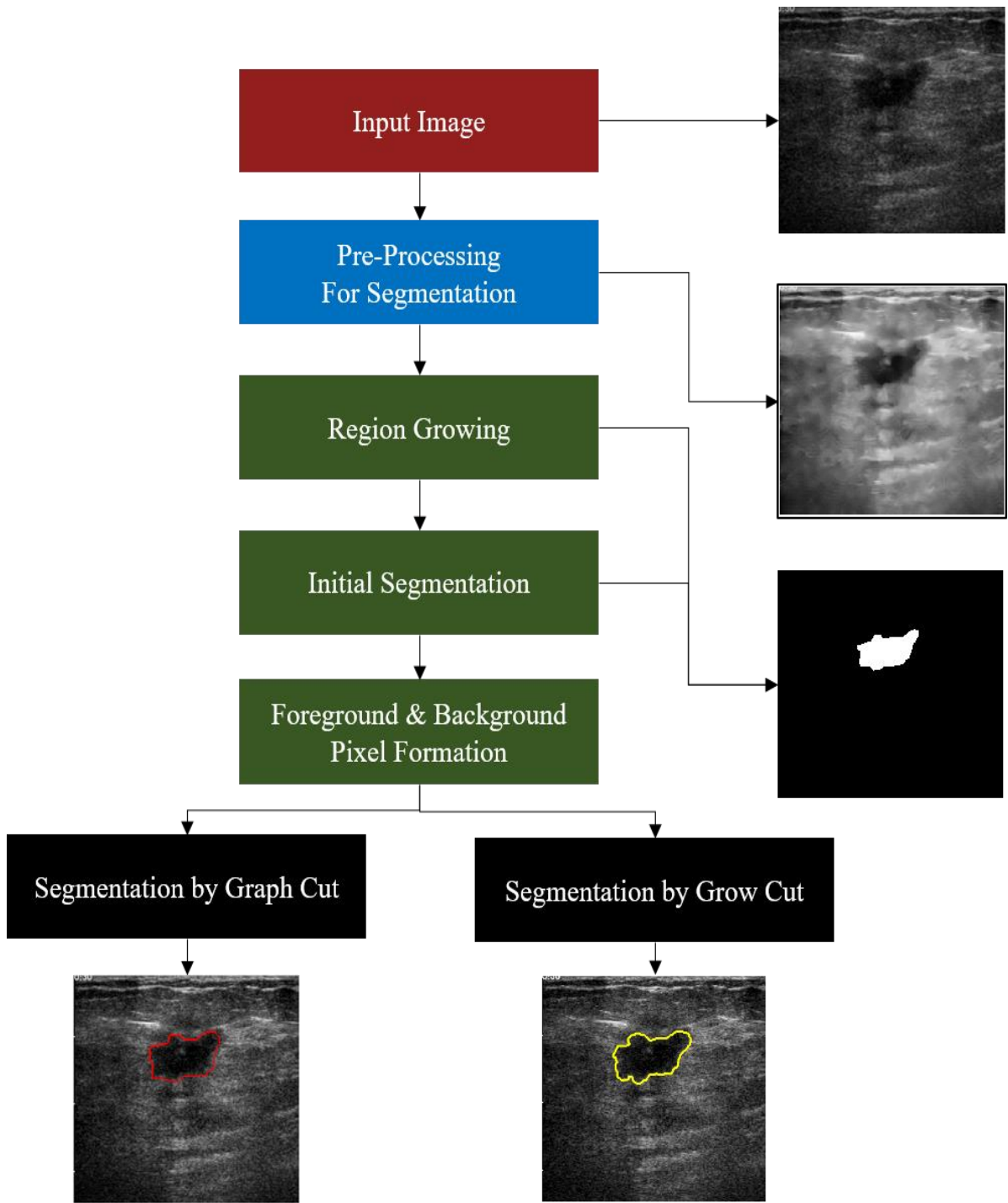


Figure 4-1 Overview of Segmentation Framework

4.1 Image Pre-processing for Segmentation

The main aim for image pre-processing is to increase homogeneity inside the tumor lesion and enhance the tumor boundary by using standard image processing techniques. The proposed image pre-processing scheme for our segmentation framework is illustrated in Figure 4-2 and discussed in details in next subsequent subsections.

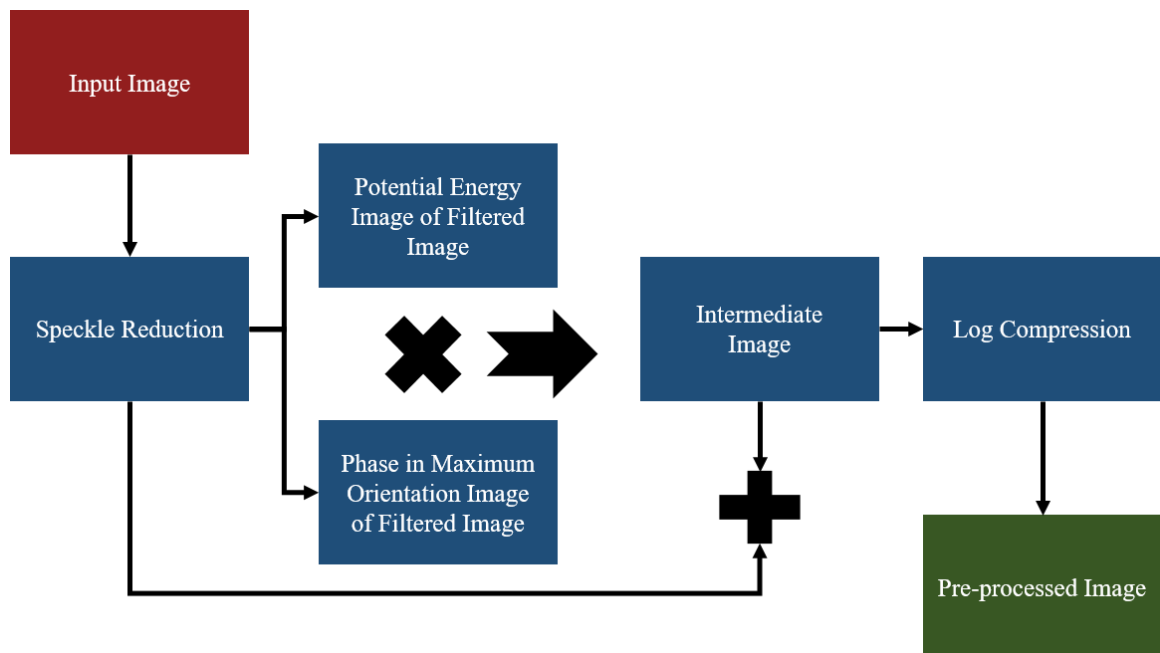
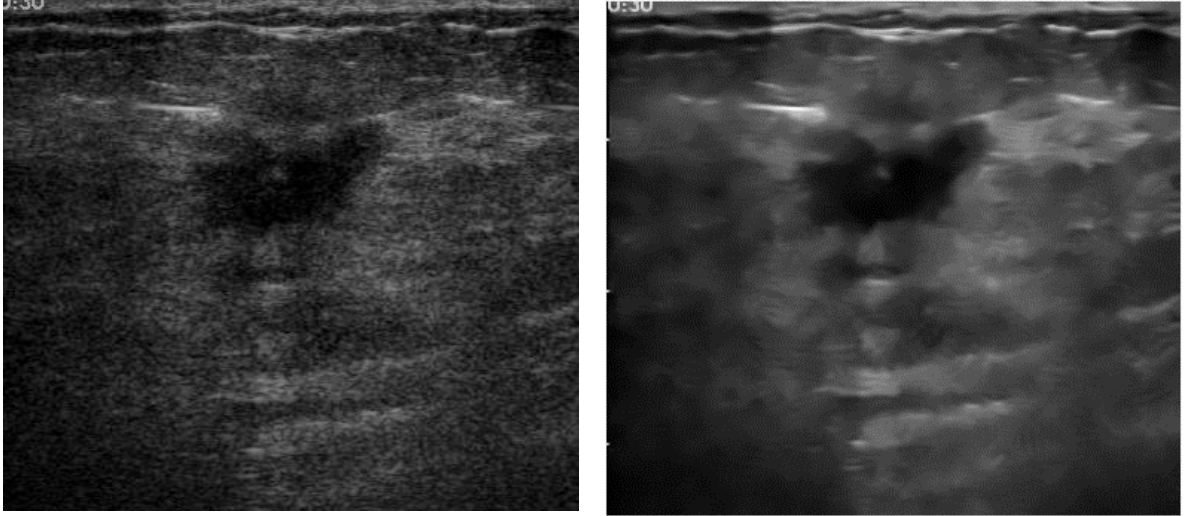


Figure 4-2 Flowchart of image pre-processing for final segmentation

4.1.1 Speckle Reduction

Speckle is a particular kind of noise which affects ultrasound images, and can significantly reduce their quality and diagnostic usefulness [30]. The main aim of ultrasound de-noising methods is both to produce of image of standard appearance with reduced level of speckle for improving the appearance of images but importantly for image analysis, both intensity inhomogeneity and speckle can challenge intensity-based segmentation methods [31]. The speckle reduction algorithm should focus reducing speckle while preserving anatomic information is necessary to delineate reliably and accurately the regions of interest and to carry on important diagnostic image analysis [32]. In our framework, we have used a recent approach for speckle reduction proposed in [32]. In [32], authors proposed an adaptation of the Non Local means (NL-means) method to a dedicated US noise model [33] using a Bayesian motivation for the NL-means filter [34]. Figure 4-3 presents the result of speckle reduction step. It is to be noted that the major anatomical details are preserved in the filtered image with a reduced level of speckle noise. The output image of the filter has less granular appearance than the original image but structure of lesion of the lesion is well preserved with increased homogeneity inside the lesion.



(a)

(b)

Figure 4-3 (a) Original Image. (b) Speckle Reduced Image

4.1.2 Potential Energy Image formation

In order to enhance the edges and introduce a level of smoothing so that spurious edges get suppressed, we generate a potential energy image described in [35]. This potential energy image is formed by using the energy functional used in Snakes [35] to produce a force that can be used to drive snakes towards features of interest inside the image such as lines, edges and terminations. The potential energy image can be expressed as a weighted combination of three functional -

$$E_{image} = w_{line}E_{line} + w_{edge}E_{edge} + w_{term}E_{term} \quad [1]$$

where, E_{image} is the potential energy image, E_{line} is region functional, E_{edge} is the edge functional and E_{term} is the termination functional. In our implementation, main goal was to introduce a slight smoothing to suppress the local and to enhance the enhance edges. Therefore, in our case, the potential energy functional contained only the region and energy

functional terms by giving zero weightage to the termination functional. The region and edge energy functional are defined [45] as –

$$E_{line} = G_{\sigma}(x, y) * I(x, y) \quad [2]$$

$$E_{edge} = |\nabla[G_{\sigma}(x, y) * I(x, y)]|^2 \quad [3]$$

In equation (13) and (14), $I(x, y)$ is the speckle reduced image, $G_{\sigma}(x, y)$ is a Gaussian blur function, σ is the standard deviation and ∇ is the gradient operator. The appropriate balance between the blurring and edge enhancement is achieved by carefully determining the value of weighting parameter w_{line} and w_{edge} respectively. In our work, the values of σ , w_{line} and w_{edge} are chosen (empirically determined) as 1.5, 2.0 and 3.5 respectively.

4.1.3 Phase in Maximum Orientation (PMO) Image Formation

The local phase has been suggested to be a more robust model for acoustic boundary detection and for characterizing edges. In order to enhance the edges and reduce inhomogeneity within the hypoechoic and anechoic regions of BUS image, we have used the energy-based phase feature PMO proposed in [36]. For generating PMO image, the original image is transferred to the frequency domain and filtered along six orientations according to the following angle filter –

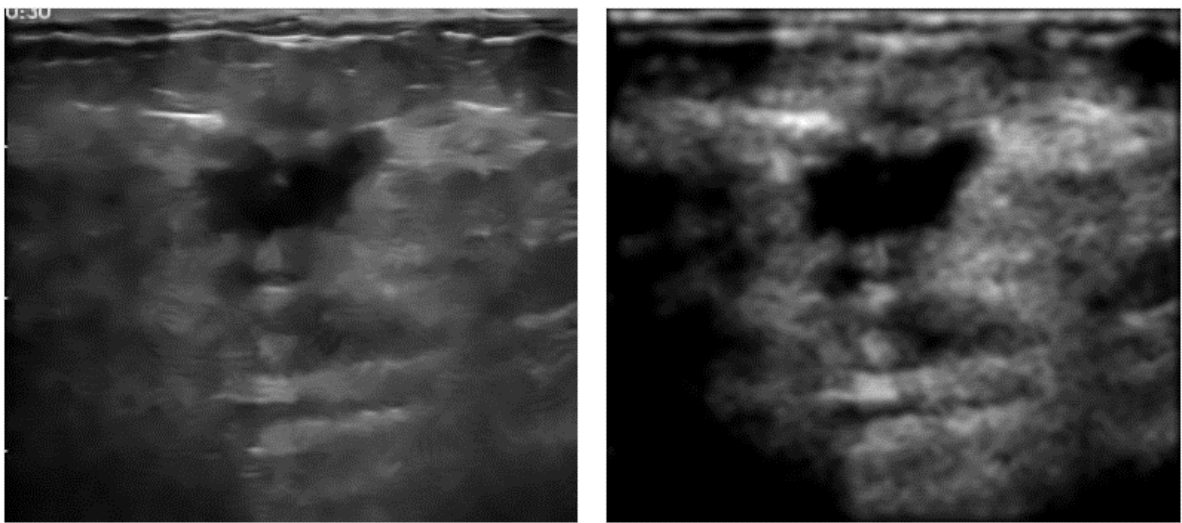
$$F_n(u, v) = \exp - \frac{(\text{atan}(-\frac{u-u_0}{v-v_0}) - \theta_n)^2}{2(\pi / 1.2N)^2} \quad [4]$$

where $\theta_n (n=1, \dots, 6)$ corresponds to six orientations, (u_0, v_0) is the origin of the frequency domain and N is the number of the orientations. Then the image is transferred back to spatial domain through inverse Fourier transform. The phase matrix PH_k and energy

matrix E_k is then saved along each orientation. For every pixel (i, j) , PMO is obtained by following formulation –

$$PMO(i, j) = PH_k(i, j), k = \operatorname{argmax}_{l=1, \dots, 6} E_l(i, j) \quad [5]$$

PMO image is then processed with three 5×5 median filter to suppress the edge responses inside the lesion in order to achieve more homogeneity in those regions. Finally, image brightness and contrast is enhanced using two brightening and intensification function proposed in [36]. Figure 4-4 shows the enhanced PMO image. The advantage of PMO is evident from the result in Figure 4-4. It is seen that the local contrast between foreground and background is enhanced, and the texture of the image becomes smoother and clearer.



(a)

(b)

Figure 4-4 (a) De-noised Image. (b) PMO image.

4.1.4 Final Processed Image Formation

An intermediate image is formed by the combination of speckle reduced image, I_{filt} ; potential energy image, E_{image} and phase in maximum orientation, $PMO(i, j)$ in the following formulation –

$$I_{int} = [E_{image} \times PMO(i, j)] + I_{filt} \quad [6]$$

Then log compression is applied on the intermediate image to get the final pre-processed image for the segmentation. Figure 4-5 illustrates final image obtained as the result of the image pre-processing for segmentation. This image is termed as pre-processed image, I_p in our work.

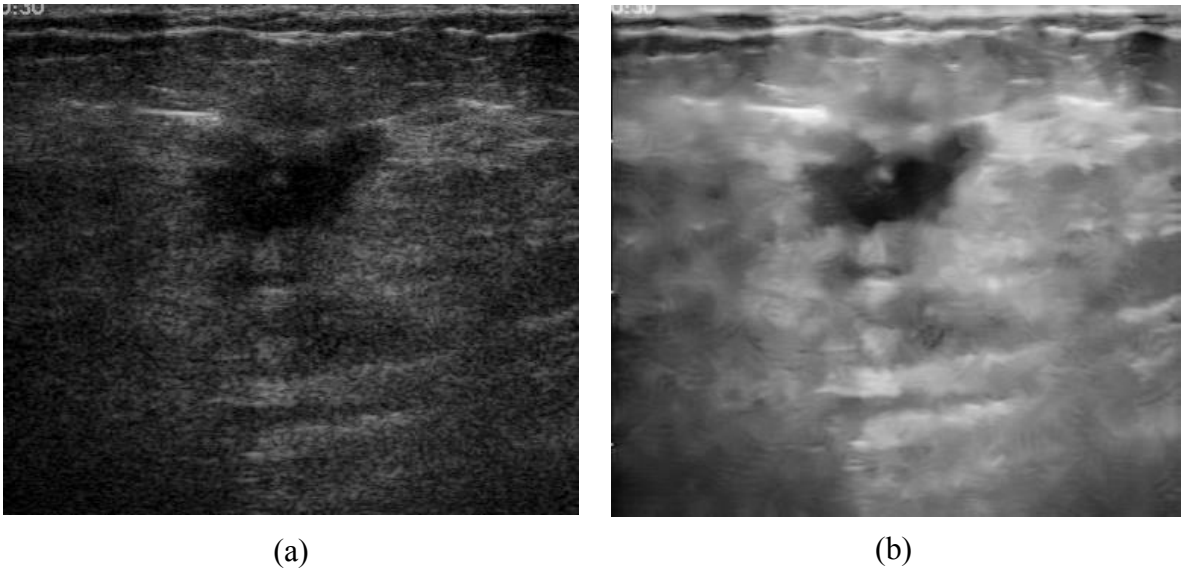


Figure 4-5 (a) Original Image. (b) Pre-processed Image

4.2 Edge Map improvement by Two-Pointers

4.2.1 Initialization region near the seed point

To solidify the results in the section, we initialize a simple region on the image, where there is a probability of the seed. The region may be a simple circle or any simple square around the region of the circle. This plot will have the segments and mostly will contain parts of the lesion area. After that we plot the histogram of the plotted area. This will help us understand what the pixel density inside the lesion region is in this specific image. The better the initialization, the histogram will prove to be more useful to use for the next step of two pointers.

4.2.2 Breaking the histogram of the total image

After the histogram reading of the lesion region, we break the histogram with two threshold values such that the most contributing values of pixels get separated from the least contributing ones. This processing is going to be done on the whole image. As the histogram can be random in shape, so we use two separation factors as of two-pointers. This two pointers separate and the new image, named the intermediate image will provide a better edge map of the image. To fill up close call edges we used the image processing tool of dilation and erosion on the image map before applying segmentation algorithm. The results of the edge map on these images are illustrated on Figure 4-6 where to show the output results simple snake segmentation method is used.

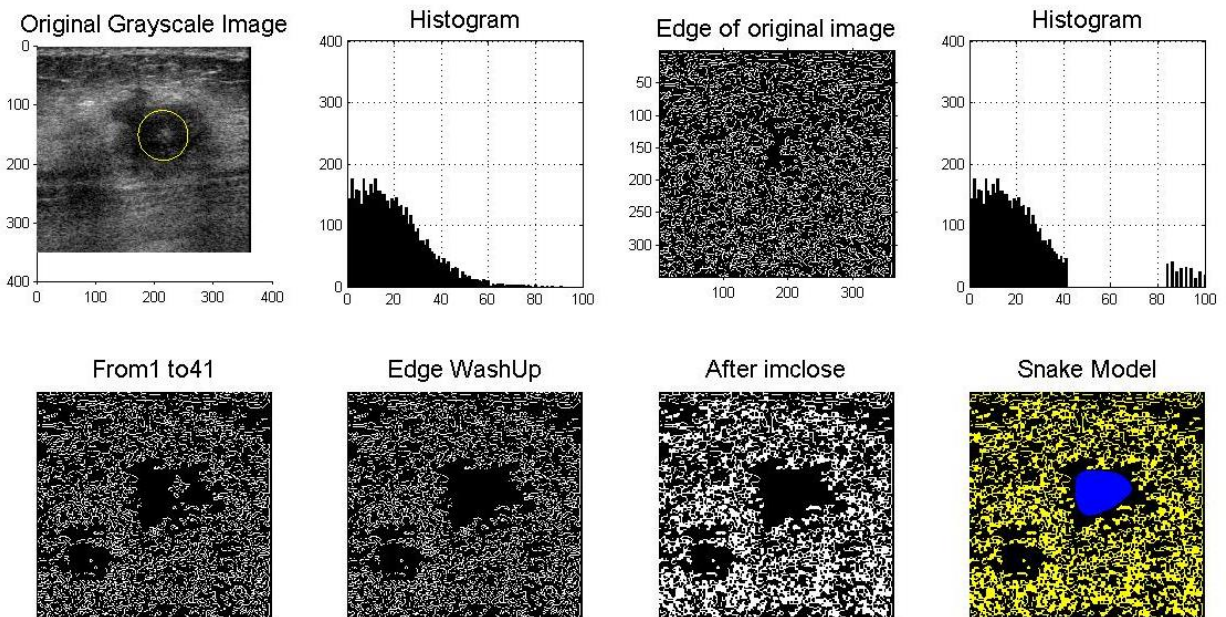
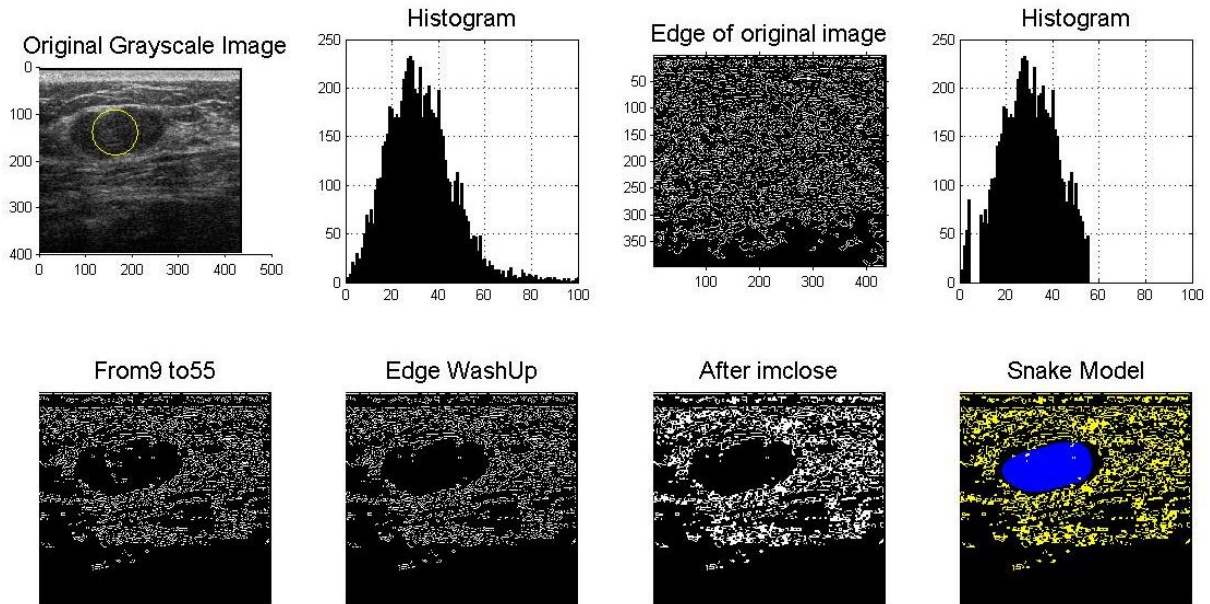
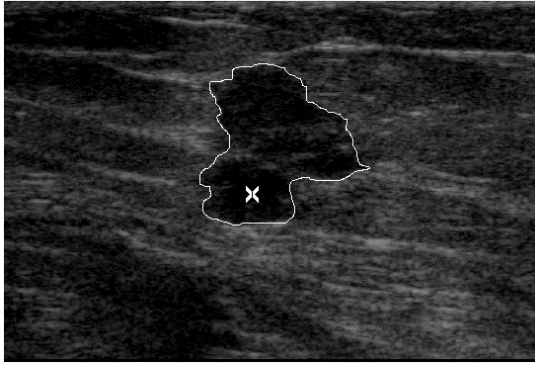


Figure 4-6 - Two Pointers processing step to obtain intermediate image with snake segmentation model

4.3 Initial Segmentation using Region Growing

Region growing is a popular segmentation method which starts from a selected seed point and adds pixels into the region by comparing their intensities with the global or local thresholds. The growing procedure stops until there are no more pixels can be added into the region. The method works well for noise-free images. However, for BUS images it cannot guarantee a good performance. In our framework, we are using region growing as a means to obtain a coarse initial segmentation based on the automatically selected seed point from the algorithm.

Many reports are found in the literature regarding the region growing for BUS images. In [14], authors used region growing as an initial guess for next subsequent processing steps. They have generated joint probability image (discussed in detail in section 3.1.4.1.1) and applied region growing on it. However, their method suffers from the problem of non-robust constraints. The stopping criterion includes two hard threshold values β_1 and β_2 which needs to be given by user. In case of BUS images due to wide range of variation of intensity, it is difficult of extract a uniform set of parameter values for larger database. This issue is evident from the images shown in Figure 4-6 obtained by region growing following the method in [14]. For all the images, the values of β_1 and β_2 are chosen as 0.4 and 2.9. It is seen in Figure 4-7 (b), using this parameter setting we are getting good initial segmentation while images in Figure 4-7 (c) and 4-7 (e) are suffering from over-segmentation with the same set of parameter.



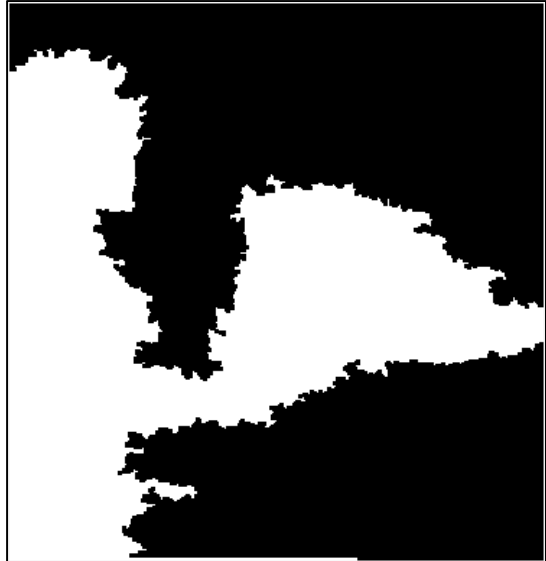
(a)



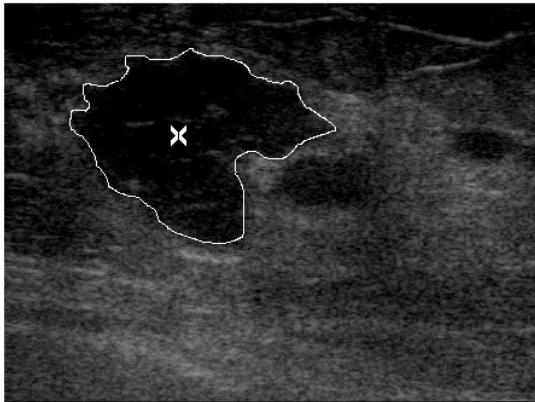
(b)



(c)



(d)



(e)



(f)

Figure 4-7 Column 1 - Original Image with manual delineation. Column 2- Region Growing using Madabhushi's method [14]

Juan Shan in [9] proposed another region growing criterion specifically for BUS images. She proposed a growing criterion which is related with both the intensity mean of the current region and the intensity mean of the entire image. The threshold was set as a dynamic value and changed from image to image. Her method produced reasonable result in comparison with Madabhusi's method [14]. However, the method suffers from over-segmentation issues in case of lesion containing leaked or weak edges. One such case is presented is Figure 4-8.

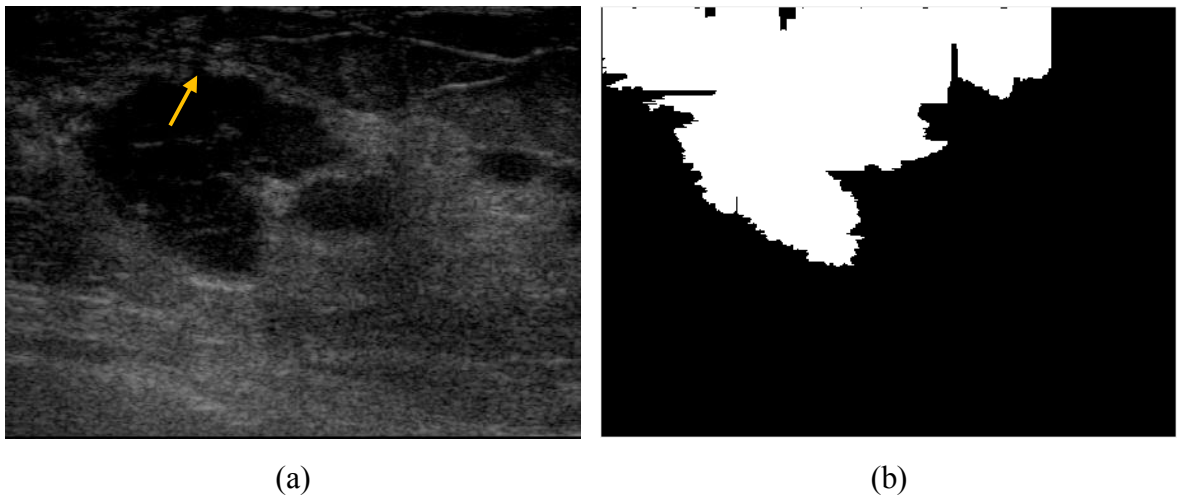


Figure 4-8 (a) Original Image with leaked edge indicated with a yellow arrow. (b) Region Growing result by Shan's method [9]

The Bus image shown in Figure 4-8 (a) has a very clear boundary except one leaked edge indicated by the yellow arrow. It is found that the Shan's region growing performs well in the area where clear boundary exists but fails if a leaked edge is present. To overcome the inconvenience of the Shan's method, in this these we are proposing a new stopping criterion for region growing.

Let R represent the set containing all the pixels in the region, and p be a pixel in R . At the beginning of region growing, set R contains only the seed point S_0 . A pixel v is included in R , if $\exists p \in R$ and it satisfies the following condition:

$$G(v) \leq \left\{ \max\left(\frac{M}{b_2}, \min(b_1 \times m, M)\right) \right\} \text{ and } \{N(p) \cap N(v) \neq \emptyset\} \text{ and } \{\nabla G(v) \leq \text{min_grad}\} \quad [7]$$

where, $G(v)$ is the intensity value of pixel v , m is the intensity mean of region R , M is the intensity mean of the entire image, and b_1 and b_2 are the parameters tuning the relationship between the stop criterion and the intensity means of the current region and the entire image, N denotes the type of connectivity of the neighborhood pixels around the pixel under consideration, ∇ is the gradient operator and min_grad is a gradient threshold used for tackling the case of leaked edges. First term of equation (18) ensures the pixels included have the similarity with the ones already included in the region while min_grad threshold introduces an additional criterion to stop region growing at the boundary of the edges regardless its strength. The equation (18) is a generalized representation of the stopping criterion used in [9]. When min_grad is set as 1, the proposed method behaves like Shan's method.

Using this modified region growing, we were able to tackle the cases the suffering from over-segmentation due to leaked edges. In our work, region growing is applied on the pre-processed image, I_p not on the original image. Figure 4-9 shows the result of growing on the image shown in Figure 4-8 (a) using the modified criterion proposed in this thesis. It is seen in Figure 4-9 (b) that the new method has the capability of reliably segment BUS images containing leaked or weak edges.

Throughout our experimentation, $b_1 = 1.2$ and $b_2 = 1.4$ was used which were determined empirically. We have used two different values for min_grad ; images with leaked edges (four cases) min_grad was set to 0.5 while for rest of the cases it was 0.9.

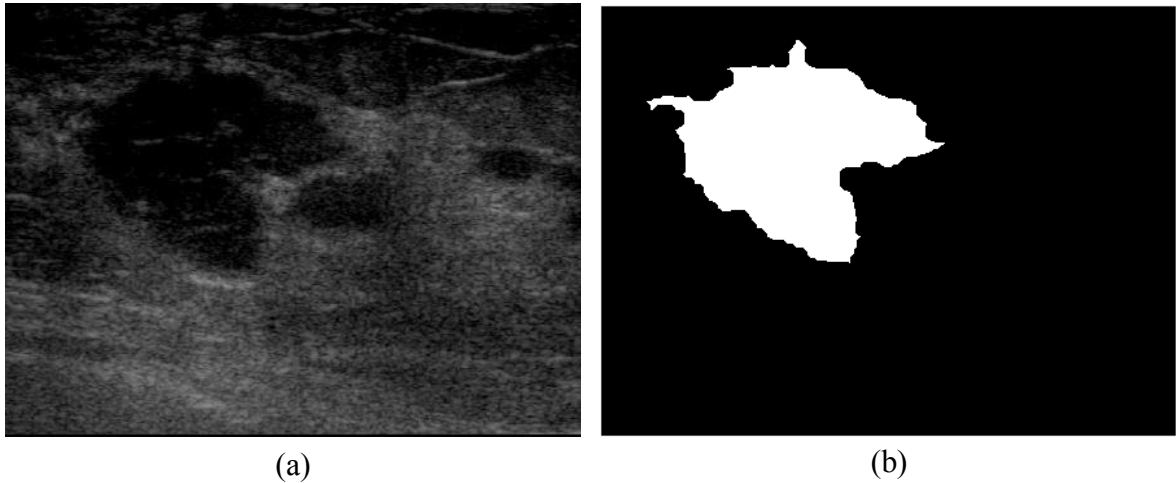


Figure 4-9 (a) Original Image. (b) Result of Region Growing proposed in this thesis

The result of the region growing, I_r will be used as a guide for generating a set of object pixels and a set of background pixels for the training of segmentation tools in next steps.

4.4 Final Segmentation

In this work, final segmentation is achieved through “GraphCut” [18] and “GrowCut” [19] segmentation. Both of the methods are interactive i.e. they require user interaction for training the algorithm with the understanding of object and background pixels. The novelty of our work is that we aim to achieve complete automation for both GraphCut and GrowCut and apply them in BUS image segmentation.

4.4.1 Graph Cuts Segmentation

In this section, the theoretical background of Graph Cuts segmentation [18] is presented.

Let P denote the set of pixels of an input image and N denote the set of adjacent pixels. Let

$A = (A_1, \dots, A_p, \dots, A_{|P|})$, be a segmentation result of the image. A_p belongs to either

object ($A_p = \text{OBJ}$) or background ($A_p = \text{BKG}$), where OBJ and BKG are labels for an object

pixel and a background pixel, respectively. In the training phase, object and background

labels are assigned to some pixels by the user. Let $E(A)$, $R(A)$, and $B(A)$ denote the energy

function, region energy, and boundary energy, respectively.

$$E(A) = \lambda \cdot R(A) + B(A) \quad [8]$$

where,

$$R(A) = \sum_{p \in P} R_p(A_p) \quad [9]$$

$$B(A) = \sum_{\{p,q\} \in N} B_{\{p,q\}} \cdot \delta(A_p, A_q) \quad [10]$$

and

$$\delta(A_p, A_q) = \begin{cases} 1 & \text{if } A_p \neq A_q \\ 0 & \text{if } A_p = A_q \end{cases} \quad [11]$$

The parameter λ reflects the weight of the region energy $R(A)$. $R(A)$ represents the

individual penalties for assigning the pixel p to OBJ and BKG, that is, $R_p(\text{OBJ})$ and

$R_p(\text{BKG})$. $R_p(\text{OBJ})$ is large when p is similar to the user-specified object, and $R_p(\text{BKG})$ is

large when p is similar to the user-specified background. The coefficient $B_{\{p,q\}}$ serves as a

penalty for a discontinuity between p and q . $B_{\{p,q\}}$ is large when p and q are similar.

In this setting, the goal of the segmentation is to solve the following optimization problem:

$$\min E(A) = \lambda.R(A) + B(A) \quad [12]$$

$$s.t. A_p = \begin{cases} \text{OBJ} & \text{if } p \in O \\ \text{BKG} & \text{if } p \in B \end{cases} \quad [13]$$

In [18], Graph cuts is proposed to as a good solution to the optimization problem. A weighted graph, $G = \langle V, E \rangle$ is defined where the vertex set, $V = P \cup \{S, T\}$, S is the OBJ terminal and T is the BKG terminal and E is the set of edges connecting these vertices. The weight of the edges are determined by regional energy, boundary energy and hard constraints from the user. It can be proven that minimum cost cut \hat{C} on graph G corresponds to the optimal segmentation of the image [18].

4.4.2 GrowCut Segmentation

GrowCut is an algorithm for interactive multilabel segmentation of N-dimensional images. Given a small number of user-labelled pixels, the rest of the image is segmented automatically by a Cellular Automaton [47]. The method details are presented below.

A (bi-directional, deterministic) cellular automaton is a triplet $A = (S; N; \delta)$, where S is a non-empty state set, N is the neighborhood system, and $\delta: S^N \rightarrow S$ is the local transition function (rule). This function defines the rule of calculating the cell's state at $t + 1$ time step, given the states of the neighborhood cells at previous time step t .

The cell state S_p in our case is actually a triplet $(l_p, \theta_p, \vec{C}_p)$ – the label l_p of the current cell, ‘strength’ of the current cell θ_p , and cell feature vector \vec{C}_p , defined by the image.

A digital image is a two-dimensional array of $k \times m$ pixels. An unlabelled image may be then considered as a particular configuration state of a cellular automaton, where cellular

space P is defined by the $k \times m$ array set by the image, and initial states for $\forall p \in P$ are set to:

$$l_p = 0, \theta_p = 0, \vec{C}_p = RGB_p \quad [14]$$

where RGB_p is the three dimensional vector of pixel's p color in RGB space. In our case, RGB_p is replaced with a one dimensional vector containing the grey level of the pre-processed image, I_p . The final goal of the segmentation is to assign each pixel one of the K possible labels.

When user starts the segmentation by specifying the segmentation seeds, the seeded cells labels are set accordingly, while their strength is set to the seed strength value. This sets the initial state of the cellular automaton. At iteration $t + 1$ cell labels l_p^{t+1} and strengths θ_p^{t+1} are updated automata evolution rule which is discussed in details in [19].

In this algorithm, pixel labelling process is considered as growth and struggle for domination of K types of bacteria. The bacteria start to spread (grow) from the seed pixels and try to occupy all the image. That is why we called the method 'GrowCut'. In our case, the value of K is two.

4.4.3 Metamorphs and Deforming Segmentation

Metamorphs model shape is embedded implicitly in a higher dimensional space of distance transforms. The Euclidean distance transform is used to embed an evolving model as the zero level set of a higher dimensional distance function. In order to facilitate notation, we consider the 2D case. Let $\Phi : \Omega \rightarrow \mathbb{R}^+$ be a Lipschitz function that refers to the distance

transform for the model shape M . By definition Ω is bounded since it refers to the image domain. The shape defines a partition of the domain: the region that is enclosed by M , $[RM]$, the background $[\Omega-RM]$, and on the model, $[\partial RM]$ (In practice, we consider a narrow band around the model M in the image domain as ∂RM). Given these definitions the following implicit shape representation is considered: $\Phi_M(x) = 0$, when $x \in \partial RM$; $+ED(x,M) > 0$, when $x \in RM$; and $-ED(x,M) < 0$, when $x \in [\Omega-RM]$, where $ED(x,M)$ refers to the min Euclidean distance between the image pixel location $x = (x,y)$ and the model M . Such treatment makes the model shape representation an “image”, which greatly facilitates the integration of boundary and region information. It also provides a feature space in which objective functions that are optimized using a gradient descent method can be conveniently used. A sufficient condition for convergence of the gradient descent methods requires continuous first derivatives. The considered implicit representation satisfies such a condition. One can prove that the gradient of the distance function is a unit vector in the normal direction of the shape. This property will make our model evolution fast. Examples of this implicit representation can be found in [Fig. (1).2]. This shape representation in 3D is similarly defined in a volumetric embedding space.

4.4.4 Automatic Training Pixel Generation for Segmentation

From the discussion presented in section 4.3.1 and 4.3.2, it is clear that both GraphCut and GrowCut requires manual interaction for initial labeling of object and background pixels. This initially labeled pixels are termed as training pixels in this thesis. In this section, we present our novel approach for generating training pixels for GraphCut and GrowCut segmentation.

For generating the training pixels, we use the result the initial segmentation result from region growing step. The following steps are followed for generating the training pixels:

- 1) The region grown result, I_r is a binary image containing one connected region corresponding to the coarse segmentation of lesion. Morphological erosion is applied on this binary image to erode away eight pixels from the boundary of the lesion region. This shrunken lesion region is termed as foreground region, F_R and used to generate object pixels for the segmentation algorithms. We randomly select 800 pixels from the foreground region, F_R and use them as the object training pixels.
- 2) Two regions enlarging the foreground region are formed; one being twice of the area of the foreground region termed as B_2 while other being 1.5 times of the area of the foreground region termed as $B_{1.5}$. The background region, B_R is defined as:

$$B_R = B_2 - B_{1.5} \quad [15]$$

If the lesion is very small then the all pixels of foreground and background regions are chosen as object and background pixels respectively. Figure 4-10 shows the training pixel generation process with intermediate results.

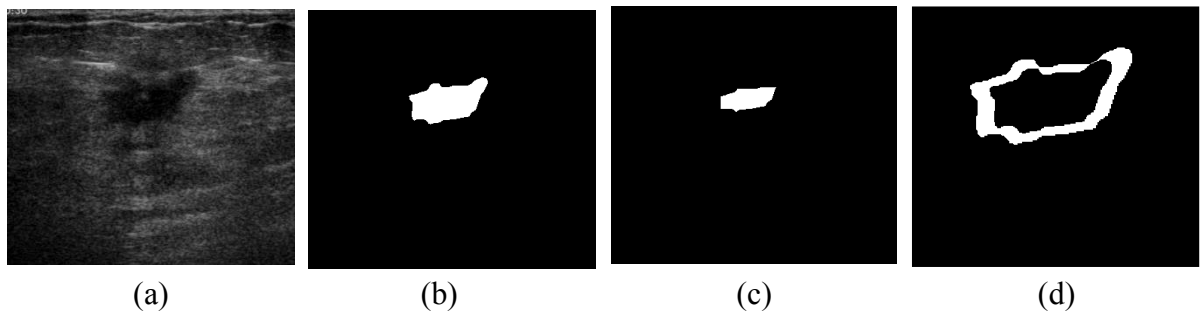


Figure 4-10 (a) Original Image. (b) Region Growing. (c) Foreground Region. (d) Background Region

4.5 Final Segmentation using GraphCut and GrowCut

In the final step of our segmentation framework, segmentation with fine detail of lesion boundary is obtained by employing GraphCut and GrowCut and also the help of metamorph segmentation on the pre-processed image, I_p . Both of the method is now completely automated as user interaction for selecting the object and background seed pixels is replaced by our proposed automatic training pixel generation. Finally, holes in the segmentation results are filled using morphological reconstruction [48], which can also be identical to the two pointers structural element as well as of the metamorphs. Figure 4-10 shows the segmentation result obtained using GraphCut as the segmentation tool while Figure 4-11 illustrates the result obtained using GrowCut as the segmentation tool.

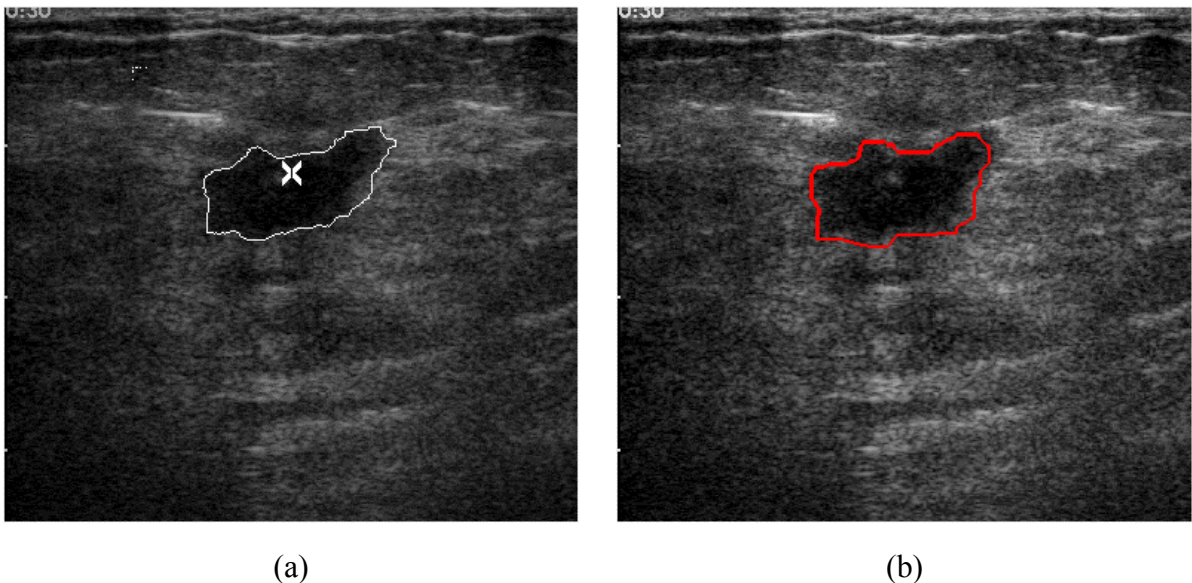


Figure 4-11 (a) Original Image with seed point and manual delineation (b) Segmentation Result using GraphCut.

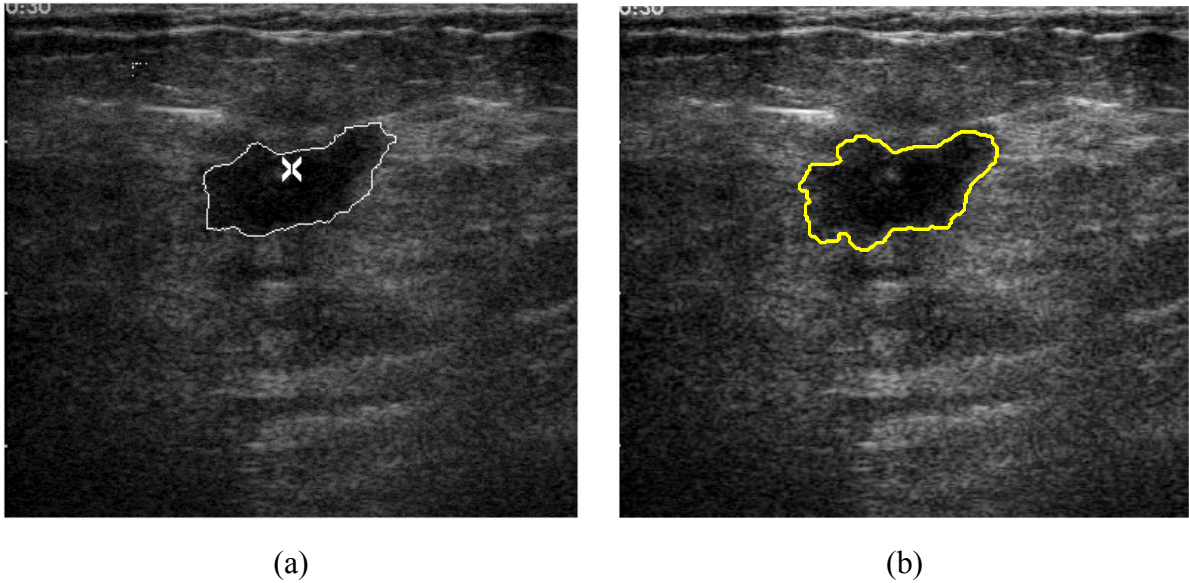


Figure 4-12 (a) Original Image with seed point and manual delineation (b) Segmentation Result using GrowCut.

5 Quantitative Ultrasound

5.1.1 Introduction

Conventional medical imaging technologies, including ultrasound, have continued to improve over the years, but the ability to classify these tissue features from images often lacks specificity. As a result, a large number of biopsies of tissues with suspicious image findings are performed each year with a vast majority of these biopsies resulting in a negative finding. To improve specificity of cancer imaging, quantitative imaging techniques can play an important role. Conventional ultrasound B-mode imaging is mainly qualitative in nature. However, quantitative ultrasound (QUS) imaging can provide specific numbers related to tissue features that can increase the specificity of image findings leading

to improvements in diagnostic ultrasound. QUS imaging can encompass a wide variety of techniques. Two very promising techniques are looked into to find possibility of improved method of tissue characterization. They are homodyne k distribution parameters and Nakagami distribution parameters.

5.1.2 Basic Functionalities

Both the method uses different approach to characterize the propagation media, in this case the propagation media is live tissue. The characterization of the propagation media is done with parametric values from this two distribution. Homodyne k provides us with information about scattered density per resolution cell and energy ratio. Nakagami distribution gives us information about effective number of scatterer and effective cross section area of scatterer. Computing these parameters for inside and outside of the region of interest (ROI) provides us with different numerical values. These values might help to distinguish between types of tissues.

5.1.3 Background and Motivation

Imaging has fundamentally transformed the practice of medicine since the first X-rays were produced more than a 100 years ago. Since that time, medical imaging techniques have continued to evolve in their capabilities, expanded in their applications and have grown in their importance to medical practice. X-ray, X-ray CT, magnetic resonance imaging (MRI), ultrasound, nuclear imaging, and optical imaging techniques have all been adapted for specific applications in medicine. Each of these imaging modalities has associated tradeoffs in terms of spatial resolution, frame rate, contrast, imaging depth, cost, safety, and portability. The improvements in biomedical imaging have, for the most part, been beneficial to the practice of medicine. For example, in recent years, the high quality of imaging has resulted in higher sensitivity to suspicious tissue features for cancer imaging and detection, although gains in sensitivity remain an important medical problem. Unfortunately, in the case of cancer, these improvements in sensitivity have not always been paralleled by improvements in specificity, i.e., the ability to determine if a suspicious

image finding is benign or malignant. As a result, a cancer “overdiagnosis” problem has occurred in which many biopsies are being conducted because of suspicious image findings with the vast majority of these biopsies having negative findings. Therefore, currently, there is a need to improve cancer imaging by improving the specificity as well as the sensitivity of imaging techniques. This in turn would reduce the number of biopsies, which would thereby reduce the cost of medical care, reduce the anxiety of, and additional risks posed to, patients undergoing these procedures, and reduce the time burden of physicians and pathologists. In order to improve the specificity of biomedical imaging, quantitative imaging techniques have been developed. A mapping of physical quantities in the image space generated from the signals can provide new sources of image contrast. In ultrasound, quantitative ultrasound (QUS) techniques include spectral-based parameterization of ultrasound signals, flow estimation through Doppler, tissue elastography techniques, shear wave imaging, and envelope statistics. Some of these techniques have already been adopted on clinical devices while some of these techniques are still under development. Our motivation is to contribute in this process. Ultrasound signals from tissues are based on the scattering of ultrasound from changes in the mechanical properties of tissue structures. Scattering from interfaces between two different kinds of tissues or large structures (on the order of a wavelength or larger) can result in large specular echoes. However, within certain tissue structures and organs, regions of uniform scattering may occur giving rise to scattering from many sub resolution structures. In B-mode, this scattering appears as speckle. Many image-processing techniques aim to reduce the presence of speckle. However, the signals giving rise to speckle are associated with the underlying tissue microstructure. Currently, the gold standard for disease classification is based on optical histology, which is able to characterize the microstructure of tissue. Therefore, if the ultrasound signals depend on tissue microstructure, then it is hypothesized that characterization of these signals could noninvasively provide information about tissue microstructure to assist in classifying disease without the need for optical histology in all cases. To properly characterize these signals, it is mandatory to model the signals associated with ultrasonic backscatter from tissues. Two methods of analyzing these

signals have gained prominence: spectral based parameterization of the signals and characterization of the envelope statistics.

5.2.1 Overview

We propose using two quantitative parameters to determine tumor characteristics.

- The Homodyne K distribution
- The Nakagami Distribution

5.2.1.1 Homodyne K:

Statistic of ultrasound signal can be used to characterize the scattering media. Scatter density and scatter type tells us that its appropriate to use the homodyne K distribution.[38]

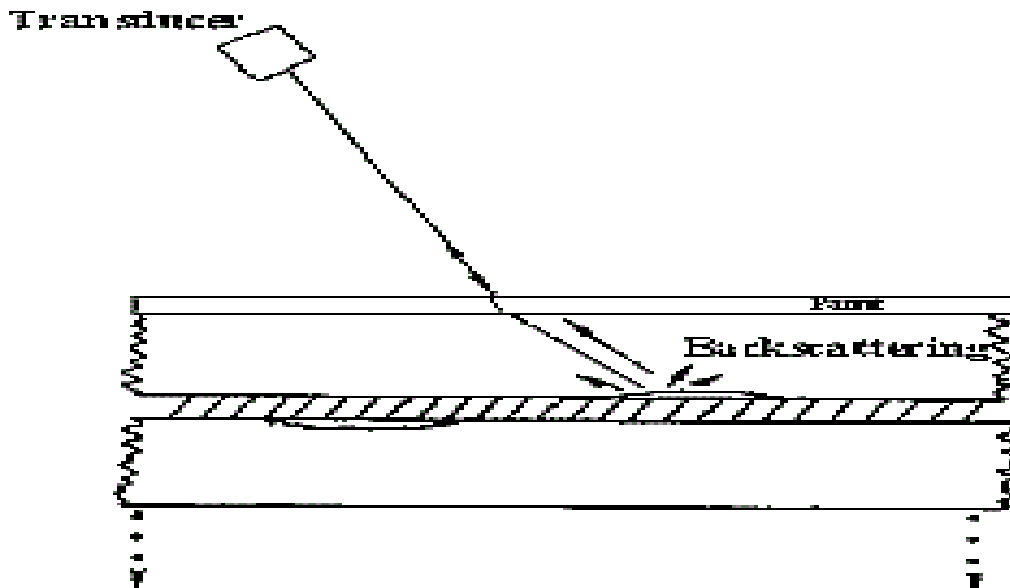


Fig: 5-1 backscattering of signal

A parameter introduced by the K distribution is the number of scatterers per resolution cell μ . The derived parameter $k = s/\sigma$ is the ratio of the coherent to diffuse signal energy and can be used to describe periodicity in scatterer locations.

5.2.1.2 Nakagami Distribution:

Nakagami distribution describes propagation condition. We intend to use “m” (effective number) and “Ω”(effective cross section), associated with the Nakagami distribution for the classification of breast masses (PM Shankar - 2001). When an acoustic pulse travels through tissue, the backscattered echo may be modeled as the algebraic sum of the contributions from the individual scatterers. If there are N scatterers, backscattered echo is

$$S(t) = \sum_{n=1}^n a \cos(\omega_j t - \theta)$$

divided into components-

$$S(t) = X \cos(\omega_j t) + Y \sin(\omega_j t)$$

$$R = \sqrt{X^2 + Y^2}$$

The Nakagami probability density function f(r), is given as:

$$F(r) = \frac{2m^m r^{2m-1}}{\Gamma(m)\Omega^m} \exp\left(-\frac{m}{\Omega} r^2\right) U(r)$$

Where, m and Ω is the nakagami parameters, Γ() is the Gamma function, U() is the unit step function. m and Ω can be found by statistical moving average.

5.3.1 Theory:

5.3.1.1 Homodyne K:

The Rayleigh Distribution: The (2-dimensional) Rayleigh distribution is defined by

$$P_{\text{Ra}}(A|\sigma^2) = \frac{A}{\sigma^2} \exp\left(-\frac{A^2}{\sigma^2}\right)$$

where A represents the amplitude of the signal. the distribution is expressed, in the context of n -dimensional random walks, in terms of the variable $a^2 = n \sigma^2$. The case σ^2 corresponds to distribution. Equivalently, the intensity I , the square of the amplitude A , is distributed according to an exponential distribution[47].

The Rice Distribution :The (2-dimensional) Rice distribution is expressed as

$$P_{\text{Ri}}(A | \varepsilon, \sigma^2) = \frac{A}{\sigma^2} I_0\left(\frac{\varepsilon}{\sigma^2} A\right) \exp\left(-\frac{(\varepsilon^2 + A^2)}{2\sigma^2}\right).$$

Where $\sigma > 0$ and $\varepsilon > 0$ are real numbers and I_0 denotes the modified Bessel function of the first kind of order 0 . The special case where ε goes to 0 yields the Rayleigh distribution. The case $n = 2$ corresponds to Nakagami .

The Homodyned K-distribution is defined by –

$$P_{\text{HK}}(A | \varepsilon, \sigma^2, \alpha) = A \int_0^\infty u J_0(u\varepsilon) J_0(uA) \left(1 + \frac{u^2 \sigma^2}{2}\right)^{-\alpha} du$$

where $\sigma > 0$, $\alpha > 0$ and $\varepsilon > 0$ and J_0 denotes the Bessel function of the first kind of order 0. the Homodyned K-distribution is expressed in terms of the parameters a , $a^2 = n\sigma^2$, and $a_0 = \varepsilon$.

The compound representation of the Homodyned K-distribution is-

$$P_{\text{HK}}(A | \varepsilon, \sigma^2, \alpha) = \int_0^\infty P_{\text{Ri}}(A | \varepsilon, \sigma^2 w) \mathcal{G}(w | \alpha, 1) dw,$$

where P_{Ri} denotes the Rice distribution and $\mathcal{G}(w | \alpha, 1)$ is the gamma distribution with mean and variance equal to α .

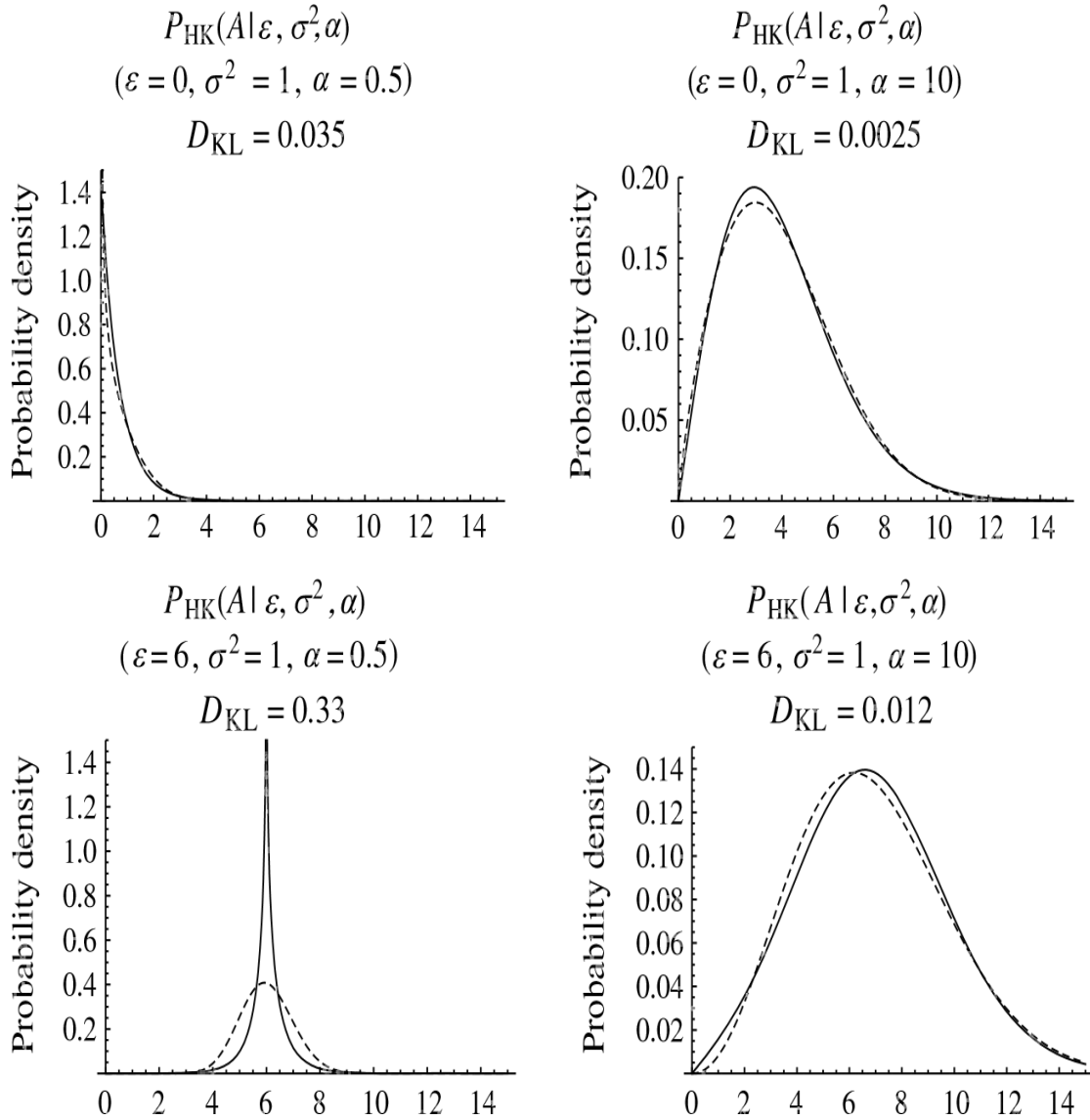


Fig: 5-2 Typical examples of the homodyned K-distribution

5.3.1.2 Nakagami Distribution:

When an acoustic pulse travels through tissue, the backscattered echo may be modeled as the algebraic sum of the contributions from the individual scatterers.

If there are N scatterers in the range cell, and a_n and θ_n represent the amplitude and the phase of the n^{th} scatterer, respectively, the backscattered echo may be written as:

$$s(t) = \sum a_n \cos(\omega_0 t - \theta_n)$$

where $\omega_0 = 2\pi f_0$, f_0 is the center frequency of insonation. The backscattered echo $s(t)$ also can be written in terms of the inphase and quadrature components, X and Y , respectively, as:

$$s(t) = X \cos(\omega_0 t) + Y \sin(\omega_0 t)$$

$$X = \sum a_n \cos(\theta_n) \text{ and } Y = \sum a_n \sin(\theta_n).$$

The envelope of the backscattered echo, R , is given by:

$$R = \sqrt{X^2 + Y^2}$$

The number density of scatterers N and the location of the scatterers play an important role in describing the statistics of the envelope of the backscattered echo. If the range cell contains a large number of randomly located scatterers, the central limit theorem can be invoked, due to which X and Y would be Gaussian distributed with zero mean and equal variance. The envelope R under this condition will obey Rayleigh statistics. The phase

$\arctan \frac{Y}{X}$) will be uniform in the range 0 to 2π . If the range cell contains scatterers that have randomly varying scattering cross sections with a comparatively high degree of variance, it was shown [39]–[40] that the Rayleigh statistics might not hold. In such cases, the inphase and quadrature components of the backscattered echo from tissue do not follow Gaussian statistics. The envelope statistics are pre-Rayleigh [41], [39]. However, if the range cell contains periodically located scatterers at spacings corresponding to integral multiples of the wavelength at the frequency of demodulation or integral multiples of half the wavelength corresponding to the demodulation frequency in addition to randomly located scatterers, the in phase and quadrature components of the backscattered echo are Gaussian with equal variance but unequal mean. The envelope statistics under these conditions are Rician or postRayleigh [42].

All these scattering conditions exist in radar and the Nakagami distribution [43] can encompass all these scattering conditions. The Nakagami probability density function $f(r)$, is given as:

In (4) $\Gamma()$ is the Gamma function and $U()$ is the unit step function. The cumulative distribution of the Nakagami distributed envelope $F(r)$ is given by:

$$F(r) = \int_0^r \frac{2m^m x^{2m-1}}{\Gamma(m)\Omega^m} \exp\left(-\frac{m}{\Omega} x^2\right) dx = P\left(\frac{m}{\Omega} r^2, m\right)$$

where $P(.,.)$ is the incomplete Gamma function. This distribution has two paramaters, namely, m and Ω . They are estimated as:

$$m = \frac{[E(R^2)]^2}{E[R^2 - E(R^2)]^2}$$

and

$$\Omega = E(R^2)$$

where $E()$ stand for statistical average. The parameter m is referred to as the Nakagami parameter and is constrained [43] such that

$$m \geq 0.5.$$

The quantity m is a shape parameter and conveys information about the envelope statistics. The parameter Ω is a scaling parameter. By substituting $m = 1$ in (4), one can observe that the density function is no different from that of a Rayleigh distribution. Thus, the case of $m = 1$, corresponds to Rayleigh scattering conditions in the range cell. If the scatterers are randomly located but have random scattering cross sections, the envelope is likely to be pre-Rayleigh [39]. In such cases, the parameter m takes values in the range of 0.5 to 1 [43], [44].

In addition to randomly located scatterers, if the range cell contains periodic scatterers separated by a spacing of an integral multiple of the wavelength (or half wavelength) corresponding to the frequency of demodulation, the backscattered echo is Rician or post-Rayleigh. The phase statistics under these conditions are essentially nonuniform. In such

cases, the value of m was shown through computer simulation to be greater than 1 [44]. In addition to the randomly located scatterers, if the range cell contains periodic scatterers spaced by an integral multiple of a quarter wavelength corresponding to the frequency of demodulation, the backscattered echo is generalized Rician [42], [44]. It was shown [44] that the value of m lies between 0.5 and 1. This situation can be separated from the pre-Rayleigh case by examining the phase statistics. The phase in the pre-Rayleigh case is uniformly distributed between 0 and 2π . However, the phase in the generalized Rician case is no uniform.

From these three cases, it is clear that the Nakagami distribution is able to encompass all these scattering conditions. However, through the preliminary studies [44], it was shown that the value of m could be less than 0.5 for scattering conditions that reflect either a low number density of scatterers or a high degree of variation in the scattering cross sections of the scatterers in the range cell. The degree of variation in the cross sections can be quantified through the signal-to-noise ratio, SNR_a , of the scattering amplitudes a , given by:

$$SNR_a = \frac{\langle a \rangle}{\sqrt{\langle a^2 \rangle - \langle a \rangle^2}}$$

A low value of SNR_a refers to a high degree of variation of scattering cross sections, and a high value refers to reasonably uniform cross sections.

These values of the parameter m less than 0.5 referred to earlier apparently seem to violate the condition [43] that m must be greater than 0.5, given in [45]. However, a closer examination of the Nakagami distribution shows that there is a direct relationship between Nakagami and Gamma density functions [43], [45]. It is possible to see that the Nakagami distribution can be identified as belonging to the class of density functions such as Gamma

distributions. If we define a new random variable $Z = R^2$, the probability density function of Z , $f(z)$ can be shown to be [46]:

$$f(z) = \frac{m^m z^{m-1}}{\Gamma(m)\Omega^m} \exp\left(-\frac{m}{\Omega} z\right) U(z), \quad m > 0.$$

The Gamma density function in with a parameter m that takes values in the range $0 < m < \infty$ instead of the limitation on m that $m \geq 0.5$. If we use the term Gamma density function in place of the Nakagami distribution, the lower limit of the value of m can be below 0.5. This dichotomy also was discussed by Nakagami in his original work [43]. Thus it is possible to have values of m lying between 0 and 0.5. These values were shown to belong to pre-Rayleigh statistics and under conditions of m being less than 0.5; the density function for $m < 0.5$ was designated to be “Nakagami-Gamma” density function [44]. In ultrasound, therefore, m can take any positive values, including values less than 0.5.

The value of m larger than 1 corresponds to Rician statistics, and other values correspond to pre-Rayleigh or generalized Rician. As described earlier, the two cases of pre-Rayleigh and generalized Rician when m lies between 0.5 and 1, can be separated by conducting a test to explore whether the phase statistics are uniform in $\{0, 2\pi\}$ or not. The phases and the envelope values are obtained after the quadrature demodulation. Table I shows the characteristic features of the Nakagami distribution in terms of the values of m , the phase statistics, and the envelope statistics designations.

Computer simulation showed that, in the absence of any periodic alignment of scatterers, the values of m were in the range of 0 to 1. As the value of m approaches unity, the statistics of the envelope approaches Rayleigh. Thus, it is possible to conclude that, when significant

variation in the scattering cross sections exist in the range cell, the envelope will be pre-Rayleigh and m will be much less than 1. In other words, m is a measure of the degree of heterogeneity (or the lack of homogeneity existing in the range cell). The greater the degree of homogeneity in tissue, the closer is the value of m to unity and vice versa. There also appears to be considerable similarity between the Nakagami parameter m and the effective number M of the K distribution [39], [40]. It was also shown [43] that the K distribution resulted from the product of two Nakagami-distributed random variables. This means that the relationship between the parameters of the K distribution (pre-Rayleigh to Rayleigh) namely, M and b [39]–[40] and the parameters of the Nakagami distribution may be obtained. Comparing the moments, we get:

$$M = \frac{2m}{1-m}$$

$$b = 2\sqrt{\frac{2m}{\Omega(1-m)}}$$

Thus m may be regarded as a measure of the effective number of scatterers in the range cell similar to M with a compressed dynamic range in the following sense—when $m \rightarrow 1, M \rightarrow \infty$, and the statistics become Rayleigh. If we define $\alpha = (1/b)$, α will be a measure of the effective cross section of the scatterers in a range cell [40]. The effective cross section α , is given by:

$$\alpha = \frac{1}{2}\sqrt{\frac{\Omega(1-m)}{2m}}$$

α can provide information about the scattering characteristics within the range cell through the parameter Ω of the Nakagami distribution. Note that this definition holds only in the pre-Rayleigh-to-Rayleigh regime ($m < 1$).

The term effective cross section is used because of the dependence of α on the number density of scatterers, signal-to-noise ratio of the cross sections (both through m), and the inhomogeneity level as well as attenuation (through both Ω or α). As a result, we may conclude that the parameter α cannot only provide information about the degree of variation in the amplitude cross sections but also on the level of attenuation present in the range cell. Thus, we expect the Nakagami distribution to be useful in tissue characterization, because these parameters, m and α , implicitly provide information on the number density of scatterers, the level of attenuation present, and the degree of homogeneity (represented by SNR_a) in the scattering cross sections.

5.4.1 Process and results:

5.4.1.1 Homodyne K :

Statistic model of ultrasound signal can be used to characterize the scattering media. The character of the scattered signal in different ways. Scatter density and scatter type tells us that it is appropriate to use the homodyne K distribution. Our body is the media in this case to be specific its soft tissue[47]. When a RF signal is sent it propagates inside the tissue depends on the scatterer present in the tissue.

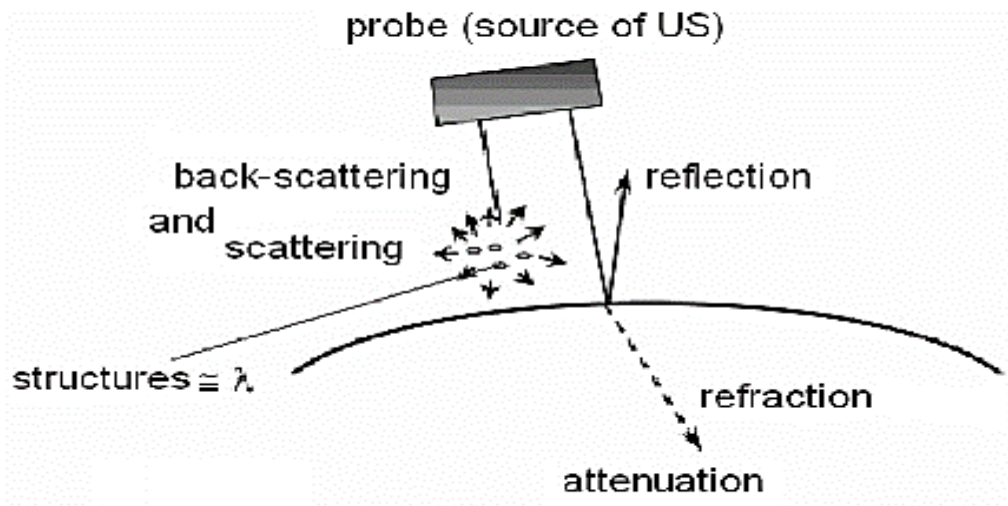


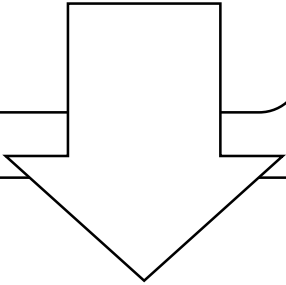
Fig : 5-3 scattering process

Only in case of a scatterer the signal will get scattered in multipath. The multipath signal when received gives valuable information about the media. In homodyne k method a parameter introduced by the K distribution is the number of scatterers per resolution cell μ . The derived parameter $k = s/\sigma$ is the ratio of the coherent to diffuse signal energy and can be used to describe periodicity in scatterer locations. For homodyne k there are two types of methods for implementation and we are going to use RHK method for our purpose.

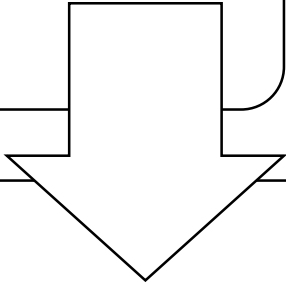
5.4.1.1.1 RSK method:

In this method we try to find the correlation between RSK values. From our back scatter signal we will calculate the RSK values (slew rate, kurtosis, signal to noise ratio). Finding the correlation from the precompiled values of RSK, homodyne k values are found.

From the back scattered signal we will calculate the estimated RSK value.



Find the points that minimizes total squared distance to precompiled RSK values



The corresponding μ and K parameters are our desired value.

μ vs K curve (result):

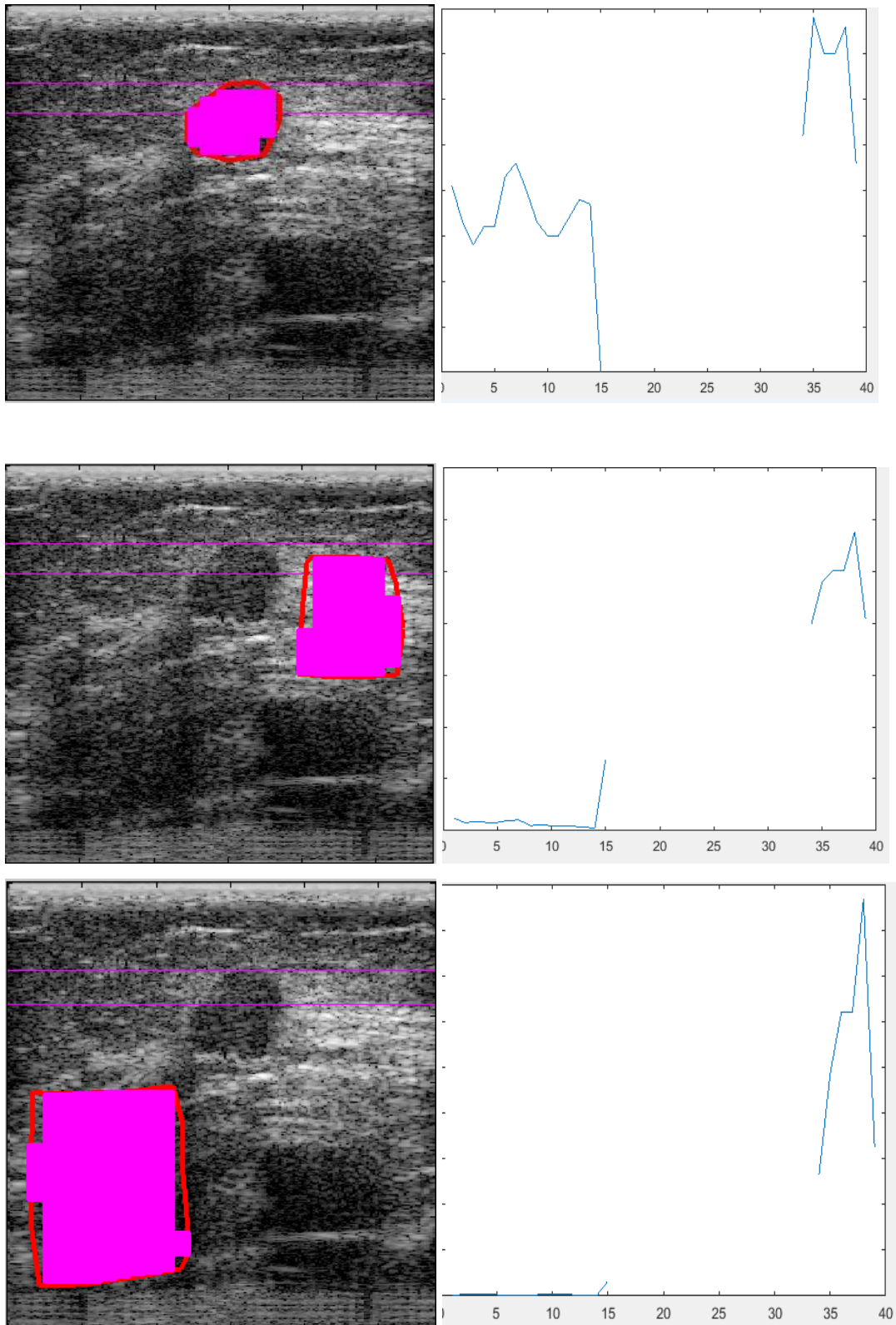


Fig : 5-4 μ vs K curve for different part of the tissue

5.4.1.2 Nakagami Distribution:

Nakagami distribution describes propagation condition. We intend to use “m” (effective number) and “ Ω ” (effective cross section), associated with the Nakagami distribution for the classification of breast masses. Back scattered signal will be fitted to a signal pattern for calculation Nakagami distribution parameters.

The signal is collected from ATL data set and windowing was done inside and outside of the ROI to get value of Nakagami parameters. It was done by fitting the distribution values.

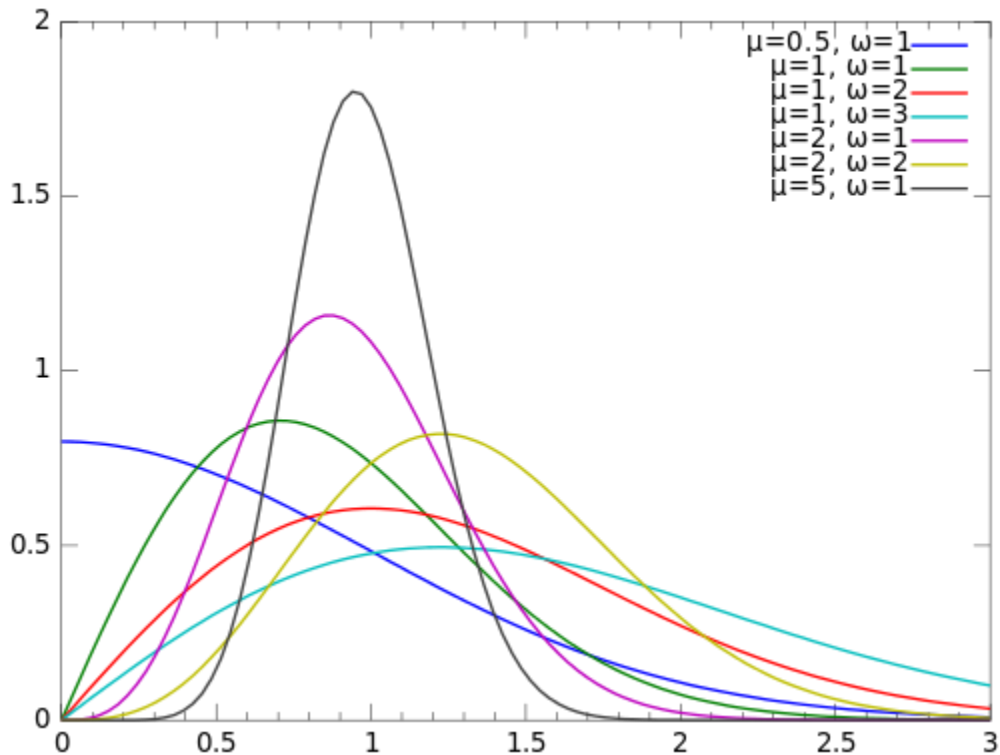


Fig : 5-5 Nakagami distribution

We can see that for different values of μ and Ω is for different type of PDF of a signal. We calculate the PDF of our signal window and correlate and from the highest correlation we calculate the value of μ and Ω .

After calculating all the value of μ and Ω we can see difference between the value of inside and outside of the ROI.

For ATL dataset the ROI was provided to us by professionals and we calculated the border line and area was defined from that with help of region growing method. Inside and outside of the ROI was treated completely differently for better results .

5.4.1.1.2 method:

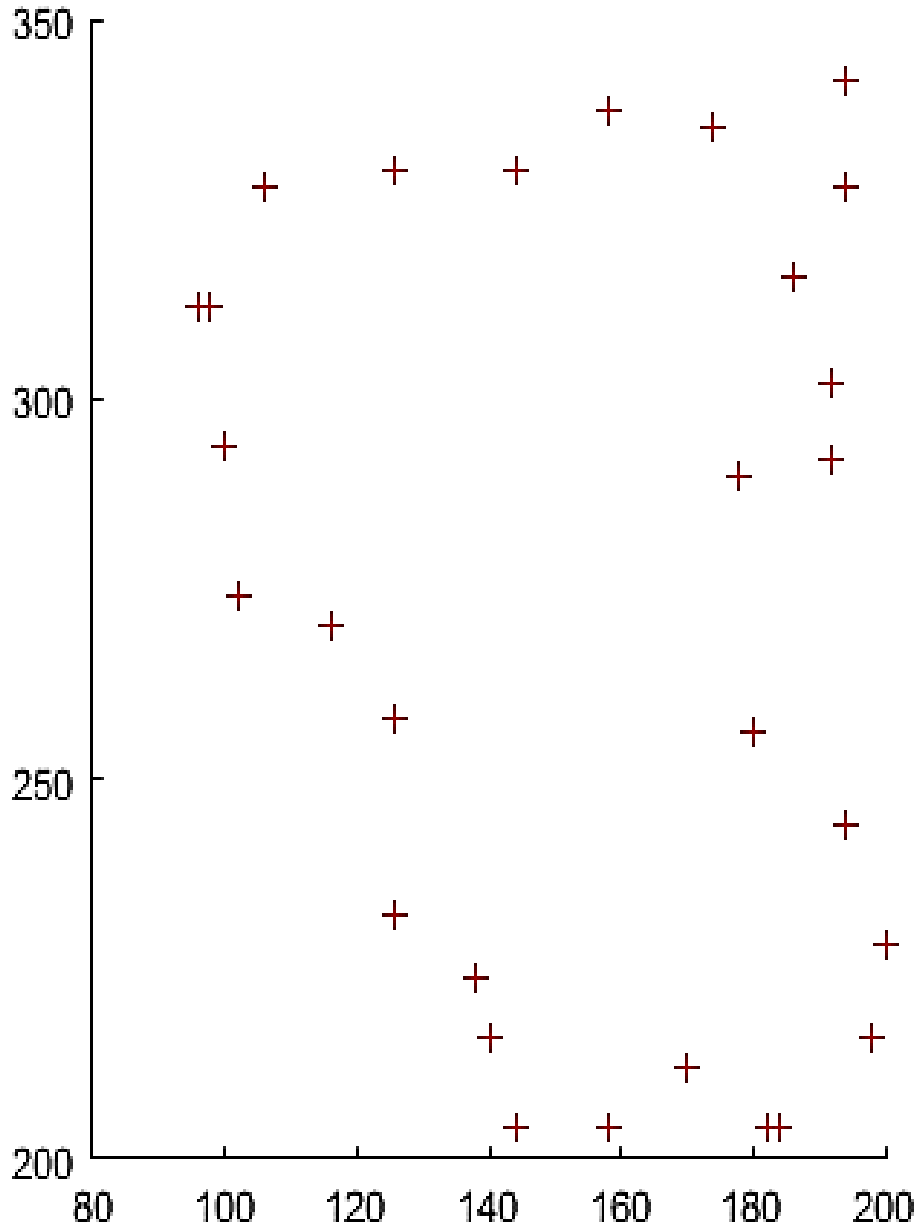


Fig : 5-6 boundary points

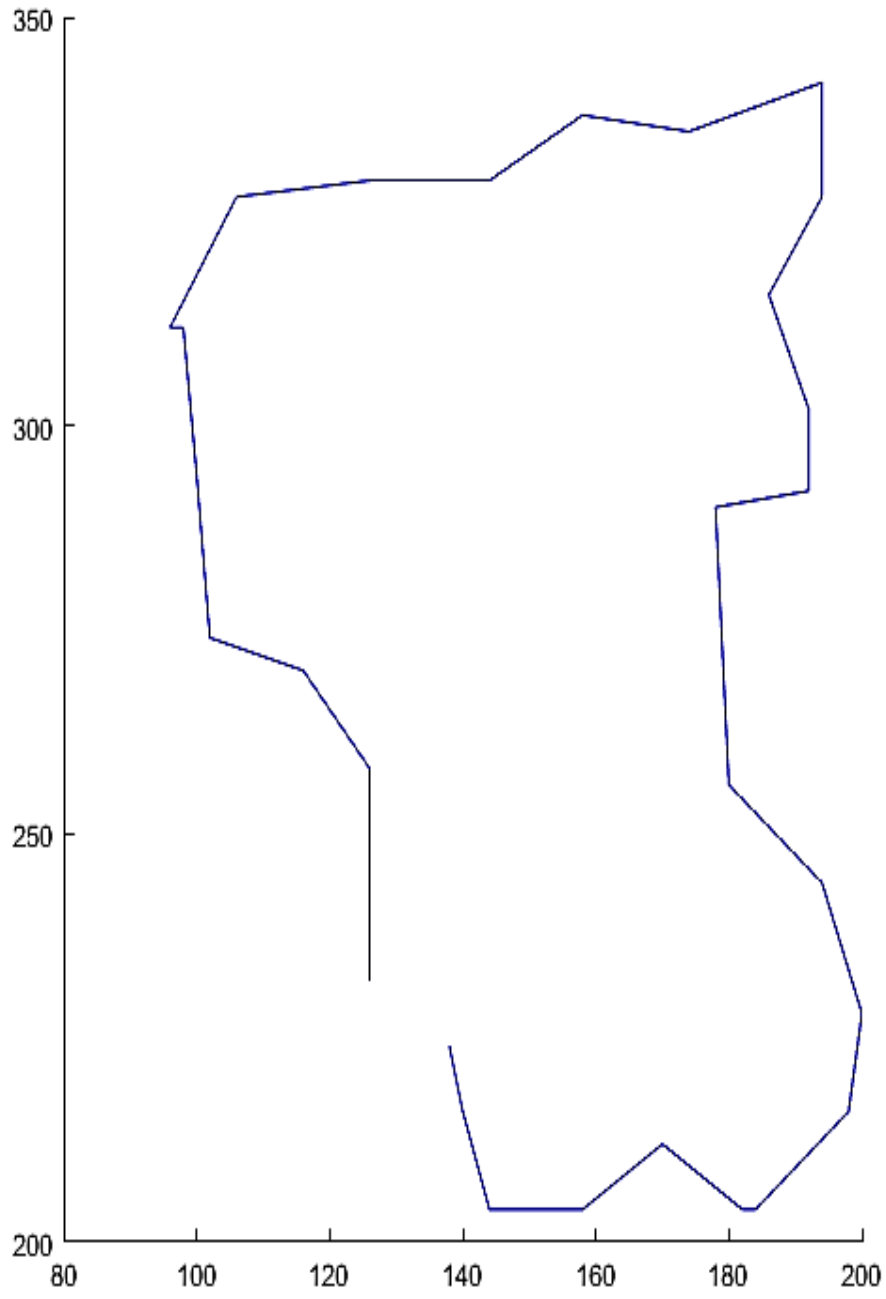


Fig :5-7 Boundary detection

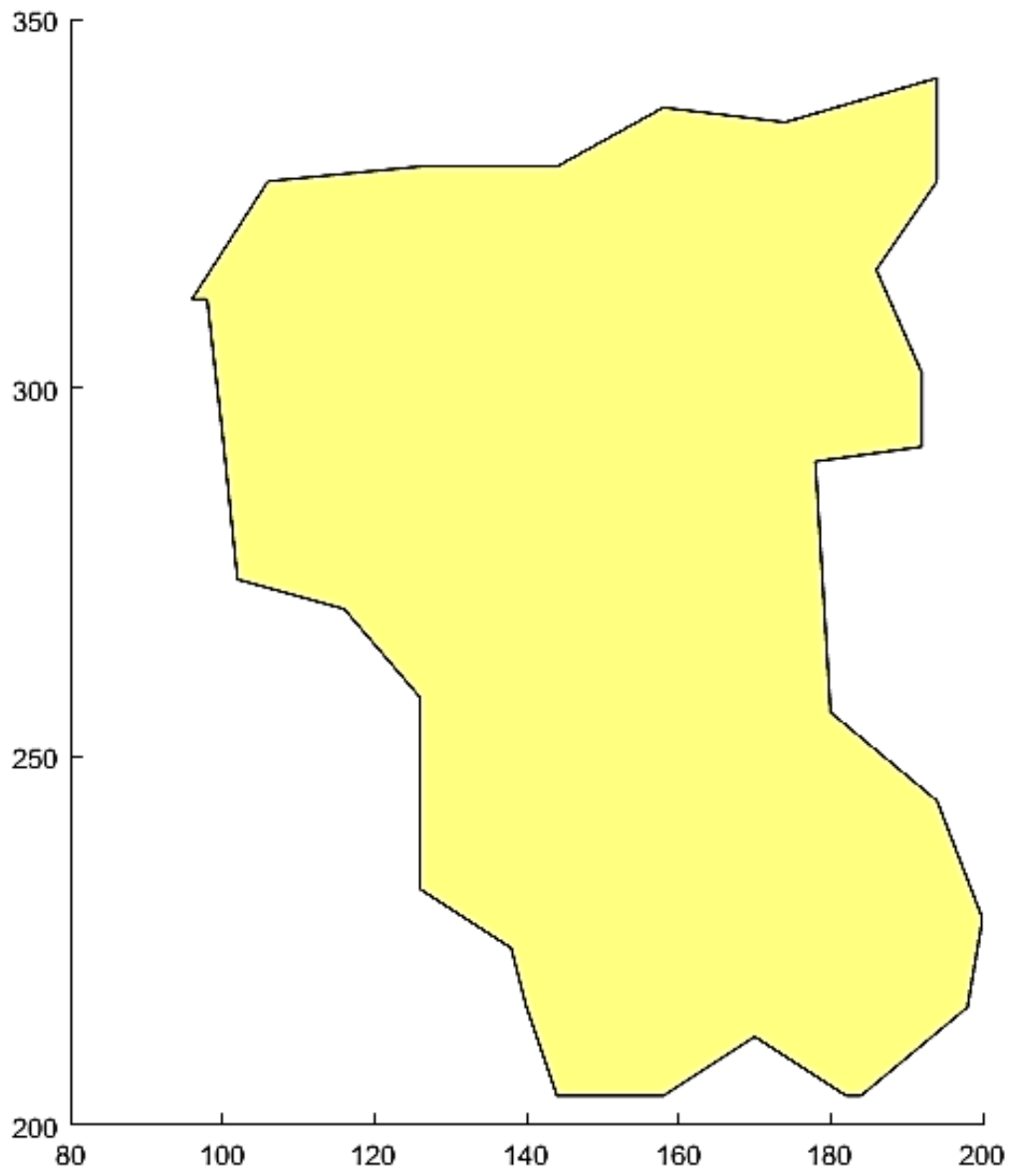


Fig :5-8 Reason of interest

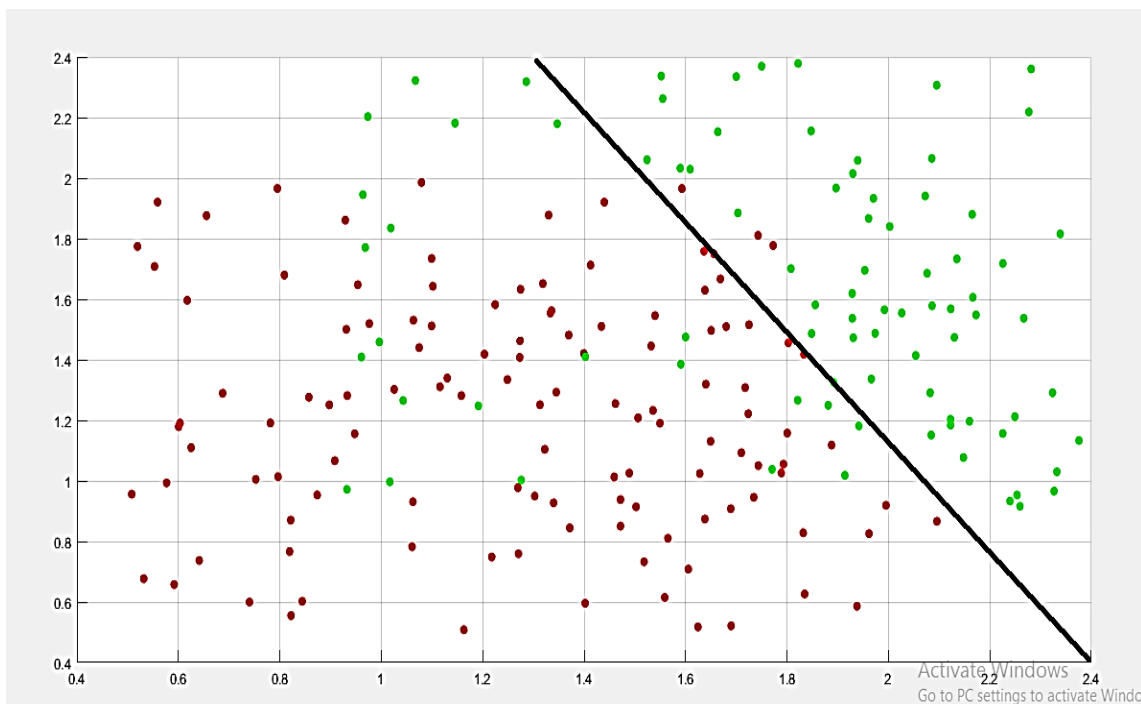
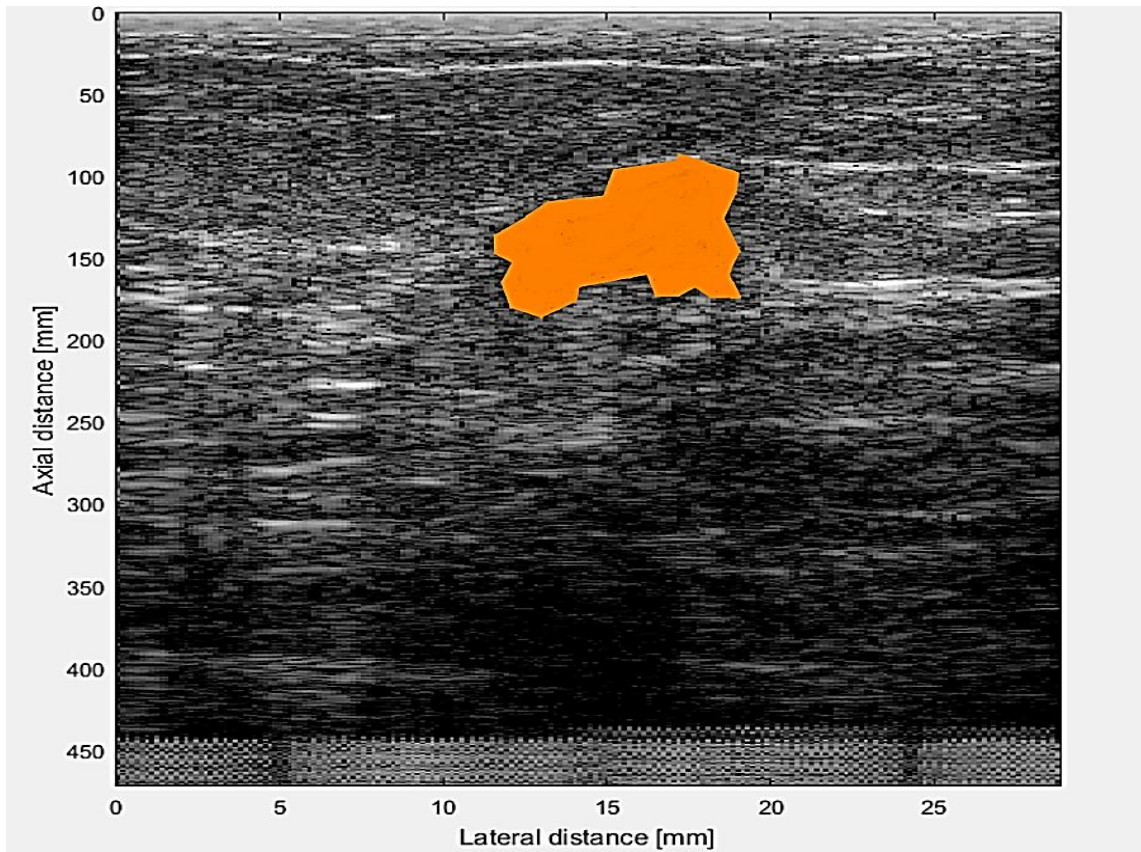


Fig : 5-9 effective number of scatterer comparison

The values inside and outside of ROI is different. Which can be a valuable information when characterizing a tissue.

6 Conclusion and Future Directions for Research

In the recent years, elastography has been widely used by the clinicians. Many clinical areas rapidly adopted the method, including prostate, liver, breast, thyroid, etc. Many new strain estimation methods have been proposed. Both 1D and 2D estimators have limitations. We have proposed a novel 1.5D method that offers a tradeoff between the two. The proposed method works well at higher strains when non-axial motion is significant. Homogeneous regions and lesions are clearly depicted, which we believe will assist radiologists in clinical situations. However, significant improvements are possible. Future work may include adaptive measurement of the lateral shift of the post-compression signal with increased efficiency and reduced complexity. We will also refine the method for optimal performance with in vivo clinical data.

The two pointer is a pre-processing step for any algorithm that depends on edges or lesion or both. Automatic segmentation is important in breast imaging. This pre-processing step has been found to improve segmentation results in BUS images if used with regular image segmentation algorithms. Using it on BUS images will improve its quality for any segmentation algorithms that depends on edge map images.

If provided with seed point, the numerical values from inside and outside of the ROI are very different .which can be used as additional information for diagnosis of tissue characteristics.

7 References

- [1] H. Cheng, J. Shan, W. Ju, Y. Guo, and L. Zhang, "Automated breast cancer detection and classification using ultrasound images: A survey," *Pattern Recognition*, vol. 43, pp. 299-317, 2010.
- [2] R. L. Siegel, K. D. Miller, and A. Jemal, "Cancer statistics, 2016," *CA: a cancer journal for clinicians*, vol. 66, pp. 7-30, 2016.
- [3] M. P. Coleman, M. Quaresma, F. Berrino, J.-M. Lutz, R. De Angelis, R. Capocaccia, et al., "Cancer survival in five continents: a worldwide population-based study (CONCORD)," *The lancet oncology*, vol. 9, pp. 730-756, 2008.
- [4] A. C. Society, "Cancer Facts & Figures 2016," American Cancer Society; 2016, Atlanta2016.
- [5] K. M. Kelly, J. Dean, W. S. Comulada, and S.-J. Lee, "Breast cancer detection using automated whole breast ultrasound and mammography in radiographically dense breasts," *European radiology*, vol. 20, pp. 734-742, 2010.
- [6] S. Shapiro, W. Venet, P. Strax, L. Venet, and R. Roeser, "Ten-to fourteen-year effect of screening on breast cancer mortality," *Journal of the National Cancer Institute*, vol. 69, pp. 349-355, 1982.
- [7] A. Jalalian, S. B. Mashohor, H. R. Mahmud, M. I. B. Saripan, A. R. B. Ramli, and B. Karasfi, "Computer-aided detection/diagnosis of breast cancer in mammography and ultrasound: a review," *Clinical imaging*, vol. 37, pp. 420-426, 2013.
- [8] R.-F. Chang, W.-J. Wu, W. K. Moon, and D.-R. Chen, "Improvement in breast tumor discrimination by support vector machines and speckle-emphasis texture analysis," *Ultrasound in medicine & biology*, vol. 29, pp. 679-686, 2003.
- [9] J. Shan, H. Cheng, and Y. Wang, "A novel segmentation method for breast ultrasound images based on neutrosophic l-means clustering," *Medical physics*, vol. 39, pp. 5669-5682, 2012.
- [10] B. Sahiner, H.-P. Chan, M. A. Roubidoux, L. M. Hadjiiski, M. A. Helvie, C. Paramagul, et al., "Malignant and Benign Breast Masses on 3D US Volumetric Images: Effect of Computer-aided Diagnosis on Radiologist Accuracy 1," *Radiology*, vol. 242, pp. 716-724, 2007.
- [11] K. Drukker, M. L. Giger, K. Horsch, M. A. Kupinski, C. J. Vyborny, and E. B. Mendelson, "Computerized lesion detection on breast ultrasound," *Medical physics*, vol. 29, pp. 1438-1446, 2002.
- [12] Y.-L. Huang, D.-R. Chen, and Y.-K. Liu, "Breast cancer diagnosis using image retrieval for different ultrasonic systems," in *Image Processing, 2004. ICIP'04. 2004 International Conference on*, 2004, pp. 2957-2960.
- [13] W. Gómez-Flores and B. A. Ruiz-Ortega, "New Fully Automated Method for Segmentation of Breast Lesions on Ultrasound Based on Texture Analysis," *Ultrasound in medicine & biology*, vol. 42, pp. 1637-1650, 2016.
- [14] A. Madabhushi and D. N. Metaxas, "Combining low-, high-level and empirical domain knowledge for automated segmentation of ultrasonic breast lesions," *IEEE transactions on medical imaging*, vol. 22, pp. 155-169, 2003.

- [15] S. K. Alam, E. J. Feleppa, M. Rondeau, A. Kalisz, and B. S. Garra, "Ultrasonic multi-feature analysis procedure for computer-aided diagnosis of solid breast lesions," *Ultrasonic imaging*, vol. 33, pp. 17-38, 2011.
- [16] P. H. Arger, C. M. Sehgal, E. F. Conant, J. Zuckerman, S. E. Rowling, and J. A. Patton, "Interreader variability and predictive value of US descriptions of solid breast masses: pilot study," *Academic radiology*, vol. 8, pp. 335-342, 2001.
- [17] B. Liu, H. Cheng, J. Huang, J. Tian, J. Liu, and X. Tang, "Automated segmentation of ultrasonic breast lesions using statistical texture classification and active contour based on probability distance," *Ultrasound in medicine & biology*, vol. 35, pp. 1309-1324, 2009.
- [18] T. A. Krouskop, D. R. Dougherty, and F. S. Vinson, "A pulsed Doppler ultrasonic system for making noninvasive measurements of the mechanical properties of soft tissue," *J. Rehabil. Res. Dev.*, vol. 24, pp. 1-8, 1987.
- [19] R. M. Lerner and K. J. Parker, "Sono-elasticity in ultrasonic tissue characterization and echographic imaging," in *Proc. 7th Eur. Comm. Workshop*, J. M. Thijssen, Ed. Nijmegen, The Netherlands, 1987.
- [20] R. M. Lerner, S. R. Huang, and K. J. Parker, "'Sonoelasticity' images derived from ultrasound signals in mechanically vibrated tissues," *Ultrason. Med. Biol.*, vol. 16, pp. 231-239, 1990.
- [21] Y. Yamakoshi, J. Sato, and T. Sato, "Ultrasonic imaging of internal vibration of soft tissue under forced vibration," *IEEE Trans. Ultrason., Ferroelect., Freq. Contr.*, vol. UFFC-47, pp. 45-53, 1990.
- [22] J. Ophir, I. Cespedes, H. Ponnekanti, Y. Yazdi, and X. Li, "Elastography: A method for imaging the elasticity in biological tissues," *Ultrason. Imaging*, vol. 13, pp. 111-134, 1991.
- [23] M. O'Donnell, A. R. Skovoroda, B. M. Shapo, and S. Y. Emelianov, "Internal displacement and strain imaging using ultrasonic speckle tracking," *IEEE Trans. Ultrason., Ferroelect., Freq. Contr.*, vol. UFFC-41, pp. 314-325, 1994.
- [24] S. K. Alam, D. W. Richards, and K. J. Parker, "Detection of intraocular pressure change in the eye using sonoelastic Doppler ultrasound," *Ultrason. Med. Biol.*, vol. 20, pp. 751-758, 1994.
- [25] K. J. Parker, L. Gao, R. M. Lerner, and S. F. Levinson, "Techniques for elastic imaging: A review," *IEEE Engineering in Medicine and Biology Magazine*, vol. 15, no. 6, pp. 52-59, 1996.
- [26] S. K. Alam, J. Ophir, and E. E. Konofagou, "An adaptive strain estimator for elastography," *IEEE Transactions on Ultrasonics, Ferroelectrics and Frequency Control*, vol. 45, no. 2, pp. 461-472, Mar. 1998
- [27] - D.N. Metaxas and Xiaolei Huang, "MetaMorphs: Deformable Shape and Texture Models."
- [28] Y. Y. Boykov and M.-P. Jolly, "Interactive graph cuts for optimal boundary & region segmentation of objects in ND images," in *Computer Vision, 2001. ICCV 2001. Proceedings. Eighth IEEE International Conference on*, 2001, pp. 105-112.
- [29] V. Vezhnevets and V. Konouchine, "GrowCut: Interactive multi-label ND image segmentation by cellular automata," in *proc. of Graphicon*, 2005, pp. 150-156.
- [30] A. Madabhushi and D. N. Metaxas, "Combining low-, high-level and empirical domain knowledge for automated segmentation of ultrasonic breast lesions," *IEEE transactions on medical imaging*, vol. 22, pp. 155-169, 2003.
- [31] J. A. Noble, N. Navab, and H. Becher, "Ultrasonic image analysis and image-guided interventions," *Interface focus*, vol. 1, pp. 673-685, 2011.

- [32] P. Coupé, P. Hellier, C. Kervrann, and C. Barillot, "Nonlocal means-based speckle filtering for ultrasound images," *IEEE transactions on image processing*, vol. 18, pp. 2221-2229, 2009.
- [33] T. Loupas, W. McDicken, and P. Allan, "An adaptive weighted median filter for speckle suppression in medical ultrasonic images," *IEEE transactions on Circuits and Systems*, vol. 36, pp. 129-135, 1989.
- [34] C. Kervrann, J. Boulanger, and P. Coupé, "Bayesian non-local means filter, image redundancy and adaptive dictionaries for noise removal," in *International Conference on Scale Space and Variational Methods in Computer Vision*, 2007, pp. 520-532.
- [35] M. Kass, A. Witkin, and D. Terzopoulos, "Snakes: Active contour models," *International journal of computer vision*, vol. 1, pp. 321-331, 1988.
- [36] D. Leucht and W. Leucht, *Teaching atlas of breast ultrasound*: Thieme, 1996.
- [37] Y. Yu and S. T. Acton, "Speckle reducing anisotropic diffusion," *IEEE Transactions on image processing*, vol. 11, pp. 1260-1270, 2002.
- [38] Shankar, P., Dumane, V., Reid, J., Genis, V., Forsberg, F., Piccoli, C. and Goldberg, B. (2001). Classification of ultrasonic B-mode images of breast masses using Nakagami distribution. *IEEE Transactions on Ultrasonics, Ferroelectrics and Frequency Control*, 48(2), pp.569-580.
- [39] P. M. Shankar, "A model for ultrasonic scattering from tissues based on K-distribution," *Phys. Med. Biol.*, vol. 40, pp. 1633– 1649, 1995.
- [40] V. M. Narayanan, P. M. Shankar, and J. M. Reid, "Non-Rayleigh statistics of ultrasonic back scattered signals," *IEEE Trans. Ultrason., Ferroelect., Freq. Contr.*, vol. 41, no. 6, pp. 845–852, Nov. 1994.
- [41] T. A. Tuthil, R. H. Sperry, and K. J. Parker, "Deviation from Rayleigh statistics in ultrasonic speckle," *Ultrason. Imag.*, vol. 10, pp. 81–89, 1988.
- [42] R. F. Wagner, M. F. Insane, and D. G. Brown, "Statistical properties of radio-frequency and envelope detected signals with applications to medical ultrasound," *J. Opt. Soc. Amer. A*, vol. 4, pp. 910–922, 1987.
- [43] M. Nakagami, "The m distribution—A general formula of intensity distribution in rapid fading," in *Statistical Methods on Radio Wave Propagation*. W. C. Hoffman, Ed. New York: Pergamon Press, 1960, pp. 3–36.
- [44] P. M. Shankar, "A general statistical model for ultrasonic scattering from tissues," *IEEE Trans. Ultrason., Ferroelect., Freq. Contr.*, vol. 47, no. 3, pp. 727–736, May 2000.
- [45] R. F. Wagner, S. W. Smith, J. M. Sandrik, and H. Lopez, "Statistics of speckle in ultrasound B-scans," *IEEE Trans.*, vol. SU-30, pp. 156–163, 1986.
- [46] A. Papoulis, *Probability, Random Variables, and Stochastic Processes*. New York: McGraw-Hill, 1991.
- [47] Cristea, A., Franceschini, E., Lin, F., Mamou, J., Cachard, C. and Basset, O. (2015). Quantitative Characterization of Concentrated Cell Pellet Biophantoms using Statistical Models for the Ultrasound Echo Envelope. *Physics Procedia*, 70, pp.1091-1095.
- [48] Oelze, M. and Mamou, J. (2016). Review of Quantitative Ultrasound: Envelope Statistics and Backscatter Coefficient Imaging and Contributions to Diagnostic Ultrasound. *IEEE Transactions on Ultrasonics, Ferroelectrics, and Frequency Control*, 63(2), pp.336-351.